## Equilateral non-Gaussian Bias at the Field Level

Divij Sharma, <sup>1, 2, \*</sup> James M. Sullivan, <sup>3, †</sup> Kazuyuki Akitsu, <sup>4</sup> and Mikhail M. Ivanov<sup>3, 2, ‡</sup>

<sup>1</sup> Department of Physics and Kavli Institute for Astrophysics and Space Research,

Massachusetts Institute of Technology, Cambridge, MA 02139, USA

<sup>2</sup> The NSF AI Institute for Artificial Intelligence and Fundamental Interactions, Cambridge, MA 02139, USA

<sup>3</sup> Center for Theoretical Physics – a Leinweber Institute,

Massachusetts Institute of Technology, Cambridge, MA 02139, USA

<sup>4</sup> Theory Center, Institute of Particle and Nuclear Studies,

High Energy Accelerator Research Organization (KEK), Tsukuba, Ibaraki 305-0801, Japan

Primordial non-Gaussianity (PNG) is a common prediction of a wide class of inflationary models. Equilateral-type PNG, generically predicted by single-field inflationary models with higher-derivative interactions, imprints subtle but measurable signatures on the large-scale distribution of matter. An important parameter of these imprints is the PNG-induced bias coefficient  $b_{\psi}$ , which quantifies how the abundance and clustering of dark matter halos and galaxies respond to mode coupling in the initial conditions. Measuring  $b_{\psi}$  is important for constraining equilateral PNG, yet it is notoriously challenging due to its degeneracy with Gaussian scale-dependent bias contributions. In this work, we present the first precision measurements of equilateral  $b_{\psi}$  for dark matter halos using effective field theory at the field level. We show that this approach disentangles PNG effects from those of the Gaussian bias by virtue of noise variance cancellation. We compare our results with the phenomenological predictions based on the Peak-Background Split model, finding some agreement at the qualitative level on the redshift and mass dependence, but poor agreement at the quantitative level. We present a fitting formula for  $b_{\psi}$  as a function of the linear bias, which can be used to set priors in PNG searches with ongoing and future galaxy surveys.

## I. INTRODUCTION

The primordial accelerated expansion of our Universe, known as cosmic inflation, is the leading theoretical framework that addresses the origin and basic properties of cosmological fluctuations. Inflationary models generically predict some small but observationally testable amount of primordial non-Gaussianity (PNG) in the statistics of the cosmological initial conditions. This motivates a program of searching for these non-Gaussian signatures in the cosmic microwave background (CMB) and large-scale structure (LSS) data on the galaxy distribution. The extraction of PNG from LSS has recently become a particularly important research topic spurred by the wealth of precision data from current and upcoming LSS surveys, such as DESI [1], Euclid [2], LSST [3], and the Roman Space Telescope [4].

The leading PNG signal is captured by the bispectrum, a Fourier image of the three-point correlation function of the primordial density fluctuations. The PNG bispectrum is characterized by its amplitude  $f_{\rm NL}$  and its shape in momentum space [5], which encodes distinctive physical processes that could operate in the early Universe. For instance, the presence of multiple light fields produces to the so-called local shape of non-Gaussianity. This scenario attracts significant attention in the context of LSS, because local PNG produces a scale-dependent modulation of the galaxy power

spectrum on large scales due to an enhanced correlation between large and small-scale structure. This effect, known as the scale-dependent bias [6], has been the leading probe used to set bounds on local PNG with LSS datasets [7–20]. The scale-dependent local PNG bias depends on a combination  $f_{\rm NL}^{\rm local}b_{\phi}$ , where  $f_{\rm NL}^{\rm local}$  is the amplitude of the skewness of the primordial density distribution, and  $b_{\phi}$  is the local PNG bias coefficient whose value depends on structure formation details. Strong constraints on local PNG are possible only if  $b_{\phi}$  is known.

Other important types of PNG are equilateral and orthogonal, which are common to single field inflationary models with higher-derivative interactions. More fundamentally, equilateral non-Gaussianity is a consequence of the spontaneous breaking of de Sitter time translations by the inflaton in single-field inflation, which can be formalized in the context of the EFT of inflation [21–23]. This makes such PNG natural from the EFT viewpoint, though such a shape can also appear in some multi-field models, e.g. [24, 25]. In what follows we focus on equilateral non-Gaussianity, though much of our discussion applies to the orthogonal shape as well.

Equilateral non-Gaussianity features a weak correlation between large and small scales, which suppresses its scale-dependent bias signature. Thus the leading observable used to constrain this model is the bispectrum of galaxies, which receives a contribution from the primordial bispectrum [26–29]. In actual cosmological searches of equilateral PNG with LSS data the scale-dependent bias is marginalized over [26, 28, 29]. This approach depends on priors on the magnitude of the equilateral scale-dependent bias, which is poorly known. In principle, a detailed knowledge of the equilateral scale-dependent

<sup>\*</sup> d\_sharma@mit.edu

<sup>†</sup> Brinson Prize Fellow

<sup>&</sup>lt;sup>‡</sup> ivanov99@mit.edu

bias may even help measure  $f_{\rm NL}$  from data, analogously to how the scale-dependent bias is used for this purpose in the context of the local PNG [30].

The only estimates of the equilateral PNG available until now are those based on the phenomenological peak-background split (PBS) model [31]. While this model provides relatively accurate predictions for the scale-dependent halo bias of local and quasi-single field PNG types, see e.g. [6, 32–70], it has not been tested for the case of the equilateral PNG. In addition, precision measurements of usual Gaussian bias parameters and higher derivative bias of DM halos [71–73] showed some departures from the predictions based on the phenomenological models. The latter case is particularly concerning because the higher derivative bias is conceptually similar to the case of the equilateral PNG bias.

Moreover, there is some difficulty in the connection between the PBS model predictions and the actual measurements of these parameters from the data. This difficulty arises because the LSS data is commonly analyzed using the effective field theory (EFT) approach [35, 74–76], where bias parameters are scheme and cutoff-dependent Wilson coefficients. The PBS model allows one to predict bias parameters only in the specific limit when the EFT cutoff is set to zero, which does not match the schemes used in the EFT codes used in actual data analyses, e.g. CLASS-PT [77, 78] or velocileptors [79–81].

Finally, the empirical halo-based models are not expected to be accurate for galaxies, as exemplified by measurements of the local PNG bias  $b_{\phi}$  based on hydrodynamical simulations [57, 86–89]. This calls for a development of a systematic framework to accurately measure the equilateral PNG biases from realistic simulations.

These arguments motivate a focused study of the equilateral PNG bias parameters aimed at obtaining realistic priors for actual data analyses. In this work, we perform such a study for the first time, focusing on the case of dark matter halos.

From the practical point of view, this measurement is complicated by the fact that the equilateral PNG signature is quite weak and degenerate with the usual Gaussian bias contributions. Specifically, the scaledependence of the equilateral PNG interpolates between a constant on large scales (degenerate with the linear bias) to a  $k^2$  on small scales, degenerate with the higherderivative bias. In addition, measurements of  $b_{\psi}$  from a limited range of wavenumbers are subject to degeneracies with other Gaussian bias contributions, e.g. from the cubic tidal operator  $\Gamma_3$ , whose low-k limit is also proportional to a  $k^2$ -type bias [90]. These degeneracies make it hard to robustly detect signatures of the equilateral PNG bias. To overcome this difficulty, in this paper we employ the field-level EFT technique [91, 92] (see also

refs. [93–109]) which has been previously used for precision measurements of EFT parameters [29, 72, 110], including the local PNG bias [66]. The key benefit of the field-level EFT is the cosmic variance cancellation by means of computing the EFT predictions for the exact initial conditions of the simulation. We show that the field-level comparison of Gaussian and non-Gaussian cosmologies offers a powerful way to isolate the equilateral PNG bias  $b_{\psi}$  in simulations.

This paper is organized as follows. Section II reviews the halo bias model in the presence of PNG, including the relevant bias parameters and transfer functions for equilateral shapes. In Section III, we describe our simulation setup with non-Gaussian initial conditions and our fitting procedure. In Section IV, we present the field-level measurements of halo bias due to equilateral PNG for various redshifts and compare them to theoretical predictions from the PBS formalism. We discuss the implications and robustness of our findings, and conclude in Section V.

## II. THEORY

In this Section, we present the theoretical framework used to model the imprint of equilateral-type primordial non-Gaussianity on the halo density field using EFT.

## A. Background

PNG is a modification of the statistical properties of the assumed Gaussian initial conditions for structure formation. Many models of inflation predict interactions of the inflaton or additional light fields, which introduce couplings between long- and short-wavelength modes [111]. These nonlinearies generate a nonzero three-point function of the primordial Bardeen potential  $\phi(\mathbf{k})$  [112]. As a result, the existence of a nonzero primordial bispectrum  $B_{\phi}(k_1, k_2, k_3)$  is a signal of PNG and an important probe of non-standard models of inflation [113, 114]. The bispectrum is defined as

$$\langle \phi(\mathbf{k}_1) \, \phi(\mathbf{k}_2) \, \phi(\mathbf{k}_3) \rangle \equiv B_{\phi}(k_1, k_2, k_3) (2\pi)^3 \, \delta_D^{(3)}(\mathbf{k}_{123}),$$
(1)

where  $\mathbf{k}_{123} = \mathbf{k}_1 + \mathbf{k}_2 + \mathbf{k}_3$  and  $\delta_D^{(3)}(x)$  is the threedimensional Dirac delta function. In what follows we will also use the primed correlation functions with the delta-function stripped off, e.g.

$$\langle \phi(\mathbf{k}_1) \phi(\mathbf{k}_2) \phi(\mathbf{k}_3) \rangle' = B_{\phi}(k_1, k_2, k_3) . \tag{2}$$

Due to statistical homogeneity and isotropy, the bispectrum depends only on the magnitudes of three wavevectors  $\mathbf{k}_1$ ,  $\mathbf{k}_2$ , and  $\mathbf{k}_3$  that form a closed triangle. We define

$$B_{\phi}(k_1, k_2, k_3) = 6A_{\phi}^4 f_{\rm NL} \frac{\mathcal{S}(k_1, k_2, k_3)}{k_1^2 k_2^2 k_3^2}.$$
 (3)

<sup>&</sup>lt;sup>1</sup> Some alternative codes are now available, incl. PYBIRD, CLASS ONE-LOOP, FOLPS and PBJ [82–85].

where  $A_{\phi}^2$  is the amplitude of the primordial power spectrum,

$$\langle \phi(\mathbf{k})\phi(\mathbf{k}')\rangle = (2\pi)^3 \delta_D^{(3)}(\mathbf{k} + \mathbf{k}') P_\phi(k, z) ,$$
 (4)

where  $P_{\phi}(k) = A_{\phi}^2/k^3$ , and  $\mathcal{S}(k_1, k_2, k_3)$  encodes the shape of the bispectrum.

Different shapes of the bispectrum encode different physics during inflation [115]. For instance, a bispectrum that peaks in the squeezed triangle configuration  $(k_1 \ll k_2 \approx k_3)$  is a feature of multi-field inflationary models, where multiple light scalar fields contribute to the dynamics. This shape is called "local" PNG,

$$S_{\text{local}}(k_1, k_2, k_3) = \frac{1}{3} \frac{k_1^2}{k_2 k_3} + 2 \text{ perms.}.$$
 (5)

Single-field models of inflation, where the inflaton is the only degree of freedom, give rise to bispectra which peak in equilateral  $(k_1 \approx k_2 \approx k_3)$  or flattened  $(k_1 \approx k_2 \approx k_3/2)$  triangles. These shapes define a type of "non-local" PNG. Such signatures can be described using a basis of two shapes - equilateral and orthogonal - parameterized by amplitudes  $f_{\rm NL}^{\rm equil}$  and  $f_{\rm NL}^{\rm ortho}$  [116, 117]. The equilateral and orthogonal shape templates are given by [5, 116]

$$S_{\text{equil}}(k_1, k_2, k_3) = \left(\frac{k_1}{k_2} + 5 \text{ perms.}\right)$$

$$-\left(\frac{k_1^2}{k_2 k_3} + 2 \text{ perms.}\right) - 2, \quad (6)$$

$$S_{\text{ortho}}(k_1, k_2, k_3) = (1+p)\frac{\Delta}{e_3} - p\frac{\Gamma^3}{e_2^2},$$
 (7)

where p = 8.52587,

$$\Delta = (k_{123} - 2k_1)(k_{123} - 2k_2)(k_{123} - 2k_3),$$

$$k_{123} = k_1 + k_2 + k_3, \quad e_2 = k_1k_2 + k_2k_3 + k_1k_3,$$

$$e_3 = k_1k_2k_3, \quad \Gamma = \frac{2}{3}e_2 - \frac{1}{3}(k_1^2 + k_2^2 + k_3^2). \tag{8}$$

In this paper, we study the equilateral bispectrum shape to characterize its imprints on large-scale structure.

An important aspect of the bispectrum shape is its squeezed limit, where one momentum becomes soft. The squeezed limit of the equilateral bispectrum reads,

$$\lim_{k \to 0} B_{\phi}^{\text{equil}}(k, q, |\mathbf{k} - \mathbf{q}|)$$

$$= 12 f_{\text{NL}}^{\text{equil}} \left( 1 - (\hat{\mathbf{q}} \cdot \hat{\mathbf{k}})^2 \right) \frac{k^2}{q^2} P_{\phi}(k) P_{\phi}(q) .$$
(9)

which can be contrasted with the local one

$$\lim_{k \to 0} B_{\phi}^{\text{local}}(k, q, |\mathbf{k} - \mathbf{q}|) = 4f_{\text{NL}}^{\text{local}} P_{\phi}(k) P_{\phi}(q). \tag{10}$$

The coupling between small-scale and large-scale modes is suppressed in the equilateral case by  $k^2/q^2$ , which

has profound consequences for structure formation, and specifically, for a scale-dependent bias.

To connect these primordial signatures to late-time observables, we must relate the primordial potential  $\phi$  to the linear matter density field in cosmological perturbation theory  $\delta_1$ . Its power spectrum is given by

$$\langle \delta_1(\mathbf{k}, z) \delta_1(\mathbf{k}', z) \rangle = (2\pi)^3 \delta_D^{(3)}(\mathbf{k} + \mathbf{k}') P_{11}(k, z) .$$
 (11)

Primordial non-Gaussianity generates a non-zero threepoint function of the  $\delta_1$ . To compute it, we use the transfer function  $\mathcal{M}$ ,

$$\delta_1(\mathbf{k}, z) = \mathcal{M}(k, z)\phi(\mathbf{k}),\tag{12}$$

$$\mathcal{M}(k,z) = \left(\frac{P_{11}(k,z)}{P_{\phi}(k)}\right)^{1/2}$$
 (13)

For notational brevity, we will suppress the explicit z-dependence in the rest of the paper. The bispectrum of  $\delta_1$  is then given by

$$\langle \delta_1(\mathbf{k}_1) \, \delta_1(\mathbf{k}_2) \, \delta_1(\mathbf{k}_3) \rangle' = f_{\text{NL}} \, B_{111}(k_1, k_2, k_3) \,, = \mathcal{M}(k_1) \, \mathcal{M}(k_2) \, \mathcal{M}(k_3) \, B_{\phi}(k_1, k_2, k_3) \,,$$
(14)

where  $B_{111}$  is the primordial contribution to the threepoint function of the linear matter field, sourced by PNG.

To study the impact of PNG at an observable level, we look at the PNG effects on halo statistics. The starting point of studying how halos trace the underlying matter field is the bias expansion. First, for Gaussian initial conditions, consider the simplest Eulerian model with the linear bias  $b_1$  to express the halo overdensity field  $\delta_h$  as

$$\delta_h(\mathbf{k}) = b_1 \, \delta(\mathbf{k}) + \epsilon(\mathbf{k}) \,, \tag{15}$$

where  $\delta$  is the nonlinear dark matter field,  $\epsilon$  is a stochastic term that does not correlate with any perturbative field, and must be present since the relation between dark matter and halos is not perfectly deterministic. If the halo field  $\delta_h$  is known,  $b_1$  can be found by minimizing the mean-square difference  $\langle |\delta_h - b_1 \delta|^2 \rangle$ , yielding

$$b_1(k) = \frac{\langle \delta_h(\mathbf{k}) \, \delta^*(\mathbf{k}) \rangle}{\langle |\delta(\mathbf{k})|^2 \rangle} \,. \tag{16}$$

The bias measured in this way is a function of k. To see how well the linear bias model works, we need to see the scales up to which  $b_1(k)$  is a constant.

In the presence of PNG, short-scale statistics are modulated by long-wavelength perturbations, and additional terms are needed in the bias expansion for halo overdensity [35, 38]. This effect is controlled by the squeezed limit of the bispectrum. To account for it, one should introduce the initial gravitational potential in the bias expansion, modulated by the squeezed limit momentum dependence. In particular, at leading order, equilateral PNG adds the field  $\psi(\mathbf{k}) \propto k^2 \phi(\mathbf{k})$  to the bias expansion with a bias parameter  $b_{\psi}$  capturing the halo response to PNG [31, 38],

$$\delta_h(\mathbf{k}) = b_1 \, \delta(\mathbf{k}) + b_{yy} f_{\text{NL}} \psi(\mathbf{k}) + \epsilon(\mathbf{k}) \,. \tag{17}$$

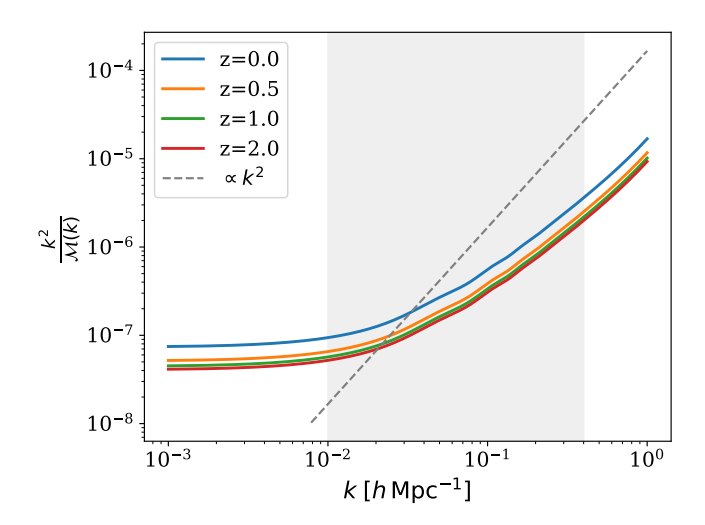


FIG. 1: Scale dependence of the equilateral PNG bias  $k^2/\mathcal{M}(k)$  at multiple redshifts. The dashed line shows the asymptotic  $k^2$  scaling. The shaded region (0.01 <  $k/h\,\mathrm{Mpc}^{-1} < 0.4$ ) indicates the range probed by galaxy surveys.

Using the transfer functions, this can be understood as a scale dependence of the linear bias parameter. We can understand it by calculating the leading contribution to the halo-matter cross-correlation spectrum,

$$P_{hm}(k) \equiv \langle \delta_h(\mathbf{k}) \, \delta(\mathbf{k}) \rangle'$$

$$= b_1 \langle \delta_1(\mathbf{k}) \, \delta_1(\mathbf{k}) \rangle' + b_\psi f_{\text{NL}} \langle \delta_1(\mathbf{k}) \, \psi(\mathbf{k}) \rangle'$$

$$= b_1 P_{11}(k) + b_\psi f_{\text{NL}} P_{1\psi}(k)$$

$$= (b_1 + \Delta b(k)) P_{11}(k). \tag{18}$$

where  $P_{1\psi}(k)$  is the cross-correlation between the matter and the  $\psi$  field.  $\Delta b(k)$  above is the scale-dependent contribution introduced by  $\psi$  to the linear bias,

$$\Delta b(k) \equiv f_{\rm NL} \, b_{\psi} \, \frac{(k/k_{\rm NL})^2}{\mathcal{M}(k)},\tag{19}$$

where we introduced the nonlinear scale of perturbation theory  $k_{\rm NL}$  for dimensional reasons.

We show the scale-dependent behavior of  $\Delta b(k)$  across redshifts in Figure 1. The shaded band indicates the range  $0.01 < k/(h\,{\rm Mpc}^{-1}) < 0.4$  that is most relevant for spectroscopic galaxy surveys. The curves show mild redshift dependence. On very large scales, the ratio flattens due to the  $k^{-2}$  scaling of  $\mathcal{M}(k)$  and behaves like a constant linear bias  $b_1$ , while at smaller scales, and in the shaded region, it asymptotically approaches a  $k^2$  behavior [31, 118].

On small scales, the PNG-induced scale-dependent bias signature is somewhat degenerate with higher-derivative operators in the bias expansion  $b_{\nabla^2\delta}\nabla^2\delta$  [30, 35, 38, 119]. Importantly, while the PNG bias is fully degenerate with  $b_1$  on large scales and with  $b_{\nabla^2\delta}$  on small scales, this degeneracy can be broken in the intermediate

transitional regime which happens to match the range of scales probed by galaxy surveys.

From the above discussion, it is natural to capture the PNG bias by promoting the bias parameters into scale-dependent transfer function  $\beta_1(k)$  as is common in EFT forward models [91]. In this approach the k-dependence of  $\beta_1(k)$  can be used to constrain the PNG-induced scale dependence and pin down  $b_{\psi}$ . With this motivation, we now turn to the full bias expansion at the one-loop order and then describe how we can use the transfer function approach to measure  $b_{\psi}$ .

## B. Halo bias expansion

The basis for our EFT forward model [91–93, 109, 120–129] is the bias expansion for the halo overdensity field  $\delta_h$  relevant at one-loop order [77, 90]. In a Universe with Gaussian initial conditions, this expansion reads

$$\delta_h(\mathbf{k})\bigg|_{\mathrm{n-pf}}^{\mathrm{EFT,G}} = b_1 \delta + \frac{b_2}{2} \delta^2 + b_{\mathcal{G}_2} \mathcal{G}_2 + b_{\Gamma_3} \Gamma_3 - b_{\nabla^2 \delta} \nabla^2 \delta + \epsilon ,$$
(20)

where we have emphasized that this is the model used to compute n-point correlation functions. In the above equations, the standard perturbation theory kernels are defined as

$$\mathcal{G}_2(\mathbf{k}) = \int_{\mathbf{p}} F_{\mathcal{G}_2}(\mathbf{p}, \mathbf{k} - \mathbf{p}) \delta(\mathbf{p}) \delta(\mathbf{k} - \mathbf{p}) , \qquad (21)$$

$$F_{\mathcal{G}_2}(\mathbf{k}_1, \mathbf{k}_2) = \frac{(\mathbf{k}_1 \cdot \mathbf{k}_2)^2}{k_1^2 k_2^2} - 1,$$
 (22)

where  $\int_{\mathbf{k}} \equiv \int \frac{d^3k}{(2\pi)^3}$ . The cubic Galileon operator  $\Gamma_3$  is defined via the kernel

$$F_{\Gamma_3} = \frac{4}{7} \left( 1 - \frac{(\mathbf{k}_1 \cdot \mathbf{k}_2)^2}{k_1^2 k_2^2} \right) \left( \frac{((\mathbf{k}_1 + \mathbf{k}_2) \cdot \mathbf{k}_3)^2}{|\mathbf{k}_1 + \mathbf{k}_2|^2 k_3^2} - 1 \right).$$
(23)

The coefficients  $b_1$ ,  $b_2$ ,  $b_{\mathcal{G}_2}$ ,  $b_{\nabla^2 \delta}$ , and  $b_{\Gamma_3}$  are free bias parameters for a given redshift and halo sample.

We emphasize that  $\delta_1$  used to construct the forward model is taken from the non-Gaussian initial conditions in the case of PNG simulations. It is also possible to use the Gaussian piece of  $\delta_1$ , but the computation of transfer functions becomes more involved in this case.

As we have seen, PNG introduces an additional scale-dependent bias to the bias expansion given in the above eq. (20) [119],

$$\delta_h(\mathbf{k}) \Big|_{\mathbf{n-pf}}^{\mathbf{EFT,NG}} = \delta_h(\mathbf{k}) \Big|_{\mathbf{n-pf}}^{\mathbf{EFT,G}} + b_{\psi} f_{\mathrm{NL}} \left(\frac{k}{k_{\mathrm{NL}}}\right)^2 \phi, \quad (24)$$

where  $k_{\rm NL} = 0.45 \, h \, {\rm Mpc}^{-1}$  is the conventional normalization scale which roughly matches the nonlinear scale and we neglect higher order corrections [72, 130].  $b_{\psi}$  in eq. (24) is an additional bias parameter of the model.

## C. Bias expansion at the field level

In order to adsorb higher order effects and minimize the dependence of the EFT forward model on small scales the bias parameters above are promoted to scaledependent transfer functions [91].

First, to account for bulk flows, the halo overdensity operators are shifted by the Zel'dovich displacement field. These *shifted operators* are defined as

$$\tilde{\mathcal{O}}(\mathbf{k}) = \int d^3q \, \mathcal{O}(\mathbf{q}) \exp\left[-i\mathbf{k} \cdot (\mathbf{q} + \psi_1(\mathbf{q}))\right],$$
 (25)

where  $\mathbf{q}$  denotes Lagrangian space (initial) coordinates,  $\mathcal{O}(\mathbf{q})$  is a Lagrangian bias operator, and  $\psi_1$  is the Zel'dovich displacement field given by

$$\psi_1(\mathbf{q}) = \int d^3k \, e^{i\mathbf{q} \cdot \mathbf{k}} \, \frac{i\mathbf{k}}{k^2} \delta_1(\mathbf{k}). \tag{26}$$

It is important to note that  $\psi_1$  has non-Gaussian correlations. To reduce degeneracies in the forward model description and ensure numerical stability, the shifted operators are orthogonalized via the Gram–Schmidt process, ensuring

$$\langle \tilde{\mathcal{O}}_m^{\perp} \tilde{\mathcal{O}}_n^{\perp} \rangle = 0 \quad \text{if} \quad n \neq m.$$
 (27)

The EFT forward model is built from the orthogonalized shifted operators

$$\delta_h^{\text{EFT}}(\mathbf{k}) = \beta_1(k)\tilde{\delta}_1(\mathbf{k}) + \beta_2(k) \left(\tilde{\delta}_1^2\right)^{\perp}(\mathbf{k}) + \beta_{\mathcal{G}_2}(k)\tilde{\mathcal{G}}_2^{\perp}(\mathbf{k}) + \beta_3(k) \left(\tilde{\delta}_1^3\right)^{\perp}(\mathbf{k}), \quad (28)$$

where  $\beta_i$  are scale-dependent transfer functions. In this approach, there is no need to introduce a separate set of transfer functions for the PNG operator  $\psi(\mathbf{k})$ ; any additional  $\beta_{\psi}(k)$  defined in this way would be degenerate with the existing  $\beta_1(k)$ .

Note that the above model contains a single cubic operator  $\delta^3$ . It is included in order to ensure that the error power spectrum, defined as

$$P_{\rm err}(k) = \langle |\delta_h^{\rm truth}(\mathbf{k}) - \delta_h^{\rm EFT}(\mathbf{k})|^2 \rangle', \qquad (29)$$

is given by the stochastic contributions at least up to the 3-loop order [91], so that one can compute it in EFT as

$$P_{\rm err} = \frac{1}{\bar{n}_h} \left( 1 + \alpha_0 + \alpha_1 \left( \frac{k}{k_{\rm NL}} \right)^2 + \dots \right) , \qquad (30)$$

where  $\bar{n}_h$  is the halo number density, and  $\alpha_{0,1}$  are stochastic EFT parameters that capture the exclusion effects [131–134].

The transfer functions are fit using the halo overdensity field from simulations,  $\delta_h^{\text{truth}}(\mathbf{k})$ ,

$$\beta_i(k) = \frac{\langle \mathcal{O}_i^{\perp *}(\mathbf{k}) \, \delta_h^{\text{truth}}(\mathbf{k}) \rangle'}{\langle |\mathcal{O}_i^{\perp}(\mathbf{k})|^2 \rangle'}. \tag{31}$$

## D. Transfer functions in EFT

Before considering the effects of PNG, we recall the form of  $\beta_1(k)$  in a Universe with Gaussian initial conditions [29], which can be predicted in perturbation theory. We get, at the one-loop order [72]

$$\beta_{1}^{G}(k) = b_{1} + b_{\nabla^{2}\delta}k^{2} + \frac{b_{2}}{2} \frac{\langle \tilde{\delta}_{1}\tilde{\delta}_{2}\rangle'}{\langle \tilde{\delta}_{1}\tilde{\delta}_{1}\rangle'} - b_{1} \frac{\langle \tilde{\delta}_{1}\tilde{\mathcal{S}}_{3}\rangle'}{\langle \tilde{\delta}_{1}\tilde{\delta}_{1}\rangle'} + \left(b_{\mathcal{G}_{2}} + \frac{2b_{1}}{7}\right) \frac{\langle \tilde{\delta}_{1}\tilde{\mathcal{G}}_{2}\rangle'}{\langle \tilde{\delta}_{1}\tilde{\delta}_{1}\rangle'} + \left(b_{\Gamma_{3}} + \frac{b_{1}}{6} + \frac{5}{2}b_{\mathcal{G}_{2}}\right) \frac{\langle \tilde{\delta}_{1}\tilde{\Gamma}_{3}\rangle'}{\langle \tilde{\delta}_{1}\tilde{\delta}_{1}\rangle'},$$

$$(32)$$

where we use the superscript "G" to note that the derivation is carried out using Gaussian initial conditions. The  $\tilde{\mathcal{S}}_3$  operator comes from the shift of the halo density field by the second-order displacement,  $\mathcal{S}_3 \equiv \psi_2 \cdot \nabla \delta_1$ . In practice, the shifted correlators above are computed using IR-resummed Eulerian time-sliced perturbation theory [72, 135–138].

With PNG, we get additional terms due to the introduction of the  $b_{\psi}$  term in eq. (24) and the PNG-induced nonzero primordial bispectrum. When cross correlating equation eq. (24) with  $\tilde{\delta}_1$ , this leads to additional terms in eq. (32). We now derive these additional terms to get our model for  $\beta_1(k)$  in the presence of PNG -  $\beta_1^{\text{NG}}(k)$ . First, we use the Eulerian kernel expansion for  $\tilde{\delta}_1$  to express it in terms of  $\delta_1$  as in [72],

$$\tilde{\delta}_1 = \sum_{m=1}^3 \left( \prod_{n=1}^m \int_{\mathbf{k}_n} \delta_1(\mathbf{k}_n) \right) (2\pi)^3 \delta_D^{(3)} \left( \mathbf{k} - \mathbf{k}_{1...m} \right) \, \tilde{K}_n. \tag{33}$$

Explicitly, the three terms in the expansion are

$$\tilde{\delta}_1^{(1)}(\mathbf{k}) = \tilde{K}_1(\mathbf{k}) \, \delta_1(\mathbf{k}),\tag{34}$$

$$\tilde{\delta}_1^{(2)}(\mathbf{k}) = \int_{\mathbf{p}} \tilde{K}_2(\mathbf{k} - \mathbf{p}, \mathbf{p}) \, \delta_1(\mathbf{k} - \mathbf{p}) \, \delta_1(\mathbf{p}), \tag{35}$$

$$\tilde{\delta}_{1}^{(3)}(\mathbf{k}) = \int_{\mathbf{p}_{1},\mathbf{p}_{2}} \tilde{K}_{3}(\mathbf{p}_{1},\mathbf{p}_{2},\mathbf{k} - \mathbf{p}_{1} - \mathbf{p}_{2})$$

$$\times \delta_{1}(\mathbf{p}_{1}) \, \delta_{1}(\mathbf{p}_{2}) \, \delta_{1}(\mathbf{k} - \mathbf{p}_{1} - \mathbf{p}_{2}), \quad (36)$$

where the kernels  $\tilde{K}_n$  are defined as

$$\tilde{K}_{1}(\mathbf{k}) = 1,$$

$$\tilde{K}_{2}(\mathbf{k}_{1}, \mathbf{k}_{2}) = 1 + \frac{1}{2} \left( \frac{\mathbf{k}_{2} \cdot \mathbf{k}_{1}}{k_{1}^{2}} + \frac{\mathbf{k}_{1} \cdot \mathbf{k}_{2}}{k_{2}^{2}} \right),$$

$$\tilde{K}_{3} = \frac{1}{2} \frac{(\mathbf{k}_{2} \cdot \mathbf{k})(\mathbf{k}_{3} \cdot \mathbf{k})}{k_{2}^{2} k_{3}^{2}}.$$
(37)

The one-loop power spectrum of  $\tilde{\delta}_1$  is given by

$$\left\langle \tilde{\delta}_{1}(\mathbf{k}) \, \tilde{\delta}_{1}(\mathbf{k}') \right\rangle' \equiv P_{\tilde{1}\tilde{1}}(k) = P_{\tilde{1}\tilde{1}}^{G}(k) + P_{12}(k), \quad (38)$$

where we have the usual expression for the Gaussian oneloop contribution

$$P_{\tilde{1}\tilde{1}}^{G}(k) = P_{11}(k) + P_{22}(k) + P_{13}(k), \tag{39}$$

with

$$P_{11}(k) \equiv \left\langle \tilde{\delta}_{1}^{(1)}(\mathbf{k}) \, \tilde{\delta}_{1}^{(1)}(\mathbf{k}') \right\rangle' = \tilde{K}_{1}^{2}(\mathbf{k}) \, P_{11}(k) = P_{11}(k), \tag{40}$$

$$P_{22}(k) \equiv \left\langle \tilde{\delta}_{1}^{(2)}(\mathbf{k}) \, \tilde{\delta}_{1}^{(2)}(\mathbf{k}') \right\rangle'$$

$$= 2 \int_{\mathbf{p}} \tilde{K}_{2}^{2}(\mathbf{k} - \mathbf{p}, \mathbf{p}) \, P_{11}(|\mathbf{k} - \mathbf{p}|) \, P_{11}(p), \qquad (41)$$

$$P_{13}(k) \equiv \langle \tilde{\delta}_{1}^{(1)}(\mathbf{k}) \, \tilde{\delta}_{1}^{(3)}(\mathbf{k}') \rangle'$$

$$= 6 \, \tilde{K}_{1}(\mathbf{k}) \, P_{11}(k) \int_{\mathbf{p}} \tilde{K}_{3}(\mathbf{p}, -\mathbf{p}, \mathbf{k}) \, P_{11}(p), \quad (42)$$

$$P_{12}(k) \equiv \left\langle \tilde{\delta}_{1}^{(2)}(\mathbf{k}) \, \tilde{\delta}_{1}^{(1)}(\mathbf{k}') \right\rangle'$$

$$= 2f_{\text{NL}} \int_{\mathbf{p}} \tilde{K}_{2}(\mathbf{k} - \mathbf{p}, \mathbf{p}) \, B_{111}(k, p, |\mathbf{k} - \mathbf{p}|). \tag{43}$$

In eqs. (38,39),  $P_{\tilde{1}\tilde{1}}^G$  is the one-loop power spectrum of the shifted field  $\tilde{\delta}_1$  under Gaussian initial conditions,  $P_{11}$  is the linear matter power spectrum,  $P_{22}$  and  $P_{13}$  are quadratic-quadratic and linear-cubic loop contributions respectively, and the  $P_{12}$  term captures a mode-coupling contribution due to the primordial bispectrum [119]. We compute the loop integrals in the above expressions with FFTLog [139] using the CLASS-PT routine [78].

Now we can calculate  $\beta_1^{NG}(k)$ . We write the crossand auto-spectra entering  $\beta_1^{NG} \equiv \langle \tilde{\delta}_1 \, \delta_h^{EFT} \rangle' / \langle \tilde{\delta}_1 \tilde{\delta}_1 \rangle'$  as a Gaussian part plus a PNG correction, so the numerator and denominator are:

$$\langle \tilde{\delta}_{1}(\mathbf{k}) \, \delta_{h}^{\text{EFT}}(\mathbf{k}) \rangle' = P_{\tilde{1}\tilde{1}}^{G}(k) \beta_{1}^{G}(k) + f_{\text{NL}} \, N(k), \qquad (44)$$
$$\langle \tilde{\delta}_{1}(\mathbf{k}) \tilde{\delta}_{1}(\mathbf{k}) \rangle' = P_{\tilde{1}\tilde{1}}^{G}(k) + f_{\text{NL}} \, D(k), \qquad (45)$$

and, from eqs. (24, 33, 38),

$$N(k) = N^{B_{111}}(k) + N^{b_{\psi}}(k), \qquad (46)$$

$$N^{B_{111}}(k) = \int_{\mathbf{p}} \left[ \frac{b_2}{2} + \left( b_{\mathcal{G}_2} + \frac{2}{7} b_1 \right) F_{\mathcal{G}_2}(\mathbf{k} - \mathbf{p}, \mathbf{p}) \right]$$

$$+ 2b_1 \widetilde{K}_2(\mathbf{k} - \mathbf{p}, \mathbf{p}) \right] B_{111}(k, p, |\mathbf{k} - \mathbf{p}|),$$

$$N^{b_{\psi}}(k) = b_{\psi} \left( \frac{k}{k_{\text{NL}}} \right)^2 \mathcal{M}^{-1}(k) \left\langle \widetilde{\delta}_1(\mathbf{k}) \widetilde{\delta}_1(\mathbf{k}) \right\rangle',$$

$$f_{\text{NL}}D(k) = P_{12}(k).$$

$$(47)$$

The first term in eq. (46) comes from the nonzero primordial bispectrum while cross correlating eqs. (24) and

(33) and the second term comes from the  $b_{\psi}$  term in eq. (24). Expanding to linear order in  $f_{\rm NL}$ ,

$$\beta_{1}^{NG}(k) = \frac{P_{\tilde{1}\tilde{1}}^{G}(k)\beta_{1}^{G}(k) + f_{NL}N(k)}{P_{\tilde{1}\tilde{1}}^{G}(k) + f_{NL}D(k)}$$

$$= \beta_{1}^{G}(k) + \underbrace{\frac{f_{NL}}{P_{\tilde{1}\tilde{1}}^{G}(k)} \Big[ N^{B_{111}}(k) - b_{1}D(k) \Big]}_{\Delta\beta_{1}(k)}$$

$$+ b_{\psi}f_{NL} \Big(\frac{k}{k_{NL}}\Big)^{2} \mathcal{M}^{-1}(k) + \mathcal{O}(f_{NL}^{2}). \tag{48}$$

The  $\Delta \beta_1(k)$  term<sup>2</sup> is given by

$$\Delta \beta_{1}(k) = \frac{f_{\text{NL}}}{P_{\tilde{1}\tilde{1}}^{G}(k)} \int_{\mathbf{p}} \left[ \frac{b_{2}}{2} + \left( b_{\mathcal{G}_{2}} + \frac{2}{7} b_{1} \right) F_{\mathcal{G}_{2}}(\mathbf{k} - \mathbf{p}, \mathbf{p}) \right]$$

$$+ 2b_{1} \widetilde{K}_{2}(\mathbf{k} - \mathbf{p}, \mathbf{p}) B_{111}(k, p, |\mathbf{k} - \mathbf{p}|)$$

$$- \frac{f_{\text{NL}} b_{1}}{P_{\tilde{1}\tilde{1}}^{G}(k)} \int_{\mathbf{p}} 2\widetilde{K}_{2}(\mathbf{k} - \mathbf{p}, \mathbf{p}) B_{111}(k, p, |\mathbf{k} - \mathbf{p}|).$$

$$(49)$$

And hence the  $b_1\widetilde{K}_2$  terms cancel. So all in all, we have

$$\beta_1^{\text{NG}}(k) = \beta_1^{\text{G}}(k) + \Delta \beta_1(k) + b_{\psi} f_{\text{NL}} \left(\frac{k}{k_{\text{NL}}}\right)^2 \mathcal{M}^{-1}(k).$$
 (50)

The terms involved in eq. (49) are the same as in the cross-spectrum between the halo and matter density fields, which is already computed CLASS-PT [26, 78], so we can get the scale dependence in the above equation from the cross-spectrum,

$$P_{hm,12}(k) = \int_{\mathbf{p}} \left[ 2b_1 \widetilde{K}_2(\mathbf{k} - \mathbf{p}, \mathbf{p}) + \frac{b_2}{2} + \left( b_{\mathcal{G}_2} + \frac{2}{7} b_1 \right) F_{\mathcal{G}_2}(\mathbf{k} - \mathbf{p}, \mathbf{p}) \right] B_{111}(k, p, |\mathbf{k} - \mathbf{p}|).$$

$$(51)$$

The subscript "12" stand for the linear-quadratic contribution to the one-loop cross-spectrum, and  $P_{hm,12}^{b_1}$ ,  $P_{hm,12}^{b_2}$ ,  $P_{hm,12}^{b_2}$  are the contributions proportional to  $b_1$ ,  $b_2$  and  $b_{\mathcal{G}_2}$  respectively.

The non-Gaussian correction to  $\beta_1$  can be re-written as

$$\Delta\beta_1(k) = \frac{f_{\rm NL}}{P_{\tilde{1}\tilde{1}}^G(k)} \left[ b_2 P_{hm,12}^{b_2}(k) + \left( b_{\mathcal{G}_2} + \frac{2}{7} b_1 \right) P_{hm,12}^{b_{\mathcal{G}_2}}(k) \right], \tag{52}$$

<sup>&</sup>lt;sup>2</sup> This is closely related to the coincidentally similarly named  $\beta_m(k)$  presented e.g. in App. A of Ref. [69] and discussed in Ref. [140].

with eq. (50) giving our model for  $\beta_1^{NG}(k)$ .

As for the other transfer functions, since our EFT forward model uses shifted operators that are orthogonalized against  $\tilde{\delta}_1$ , so that by construction  $\langle (\tilde{\delta}_1^2)^{\perp} \tilde{\delta}_1 \rangle' = 0$  and  $\langle \tilde{\mathcal{G}}_2^{\perp} \tilde{\delta}_1 \rangle' = 0$ , and when we project the halo field onto the orthogonal subspace to extract  $\beta_2$  and  $\beta_{\mathcal{G}_2}$ , the  $b_{\psi}$  term drops out:

$$\langle \delta_{h}^{\text{EFT}} (\tilde{\delta}_{1}^{2})^{\perp} \rangle' \supset f_{\text{NL}} b_{\psi} \left(\frac{k}{k_{\text{NL}}}\right)^{2} \mathcal{M}^{-1}(k) \underbrace{\langle \tilde{\delta}_{1} (\tilde{\delta}_{1}^{2})^{\perp} \rangle'}_{=0} = 0,$$

$$\langle \delta_{h}^{\text{EFT}} \tilde{\mathcal{G}}_{2}^{\perp} \rangle' \supset f_{\text{NL}} b_{\psi} \left(\frac{k}{k_{\text{NL}}}\right)^{2} \mathcal{M}^{-1}(k) \underbrace{\langle \tilde{\delta}_{1} (\tilde{\delta}_{1}^{2})^{\perp} \rangle'}_{=0} = 0.$$

$$(53)$$

Therefore, to linear order in  $f_{NL}$  and at the order we are interested in,  $\beta_2(k)$  and  $\beta_{\mathcal{G}_2}(k)$  are unaffected by  $b_{\psi}$  and we get their usual form [29],

$$\beta_2(k) = \frac{b_2}{2},\tag{54}$$

$$\beta_{\mathcal{G}_2}(k) = b_{\mathcal{G}_2} + \frac{2}{7}b_1. \tag{55}$$

## III. SIMULATIONS AND FITTING

In this Section, we describe the numerical simulations and fitting methodology that we use in our analysis to measure  $b_{\psi}$ . We describe the PNG simulations as well as other simulations used to quantify uncertainties in section III A. We then outline our field-level fitting procedure, where transfer functions are extracted from our forward model and fitted to measure  $b_{\psi}$ , in section III B.

## A. Simulations

We utilize a suite of four N-body simulations with equilateral PNG ran using the GADGET-4 code [141]. As a control suite, we also use four Gaussian simulations with the same initial seeds as our PNG simulations.

To amplify the PNG signal and practically measure the PNG bias [30], these simulations are initialized with a large equilateral PNG amplitude of  $f_{\rm NL}=1000$  with the modified version of 2LPTIC [33, 142]. Each simulation evolves  $1536^3$  dark matter particles in a periodic box of side length  $L=1\,h^{-1}{\rm Gpc}$ , resulting in a particle mass of  $\approx 2.4\times 10^{10}\,h^{-1}M_{\odot}$ . The cosmological parameters used for these simulations are: h=0.6766,  $A_s=2.105\times 10^{-9}$ ,  $n_s=0.9665$ ,  $\Omega_m=0.309$ ,  $\Omega_b=0.049$ ,  $k_{\rm pivot}=0.05\,{\rm Mpc}^{-1}$ ,  $T_{\rm CMB}=2.725\,{\rm K}$ . To identify dark matter halos, we use the ROCKSTAR [143] phase-space halo finder. We use a variety of halo mass bins, and they are noted in section IV. In the left panel of figure 4, we show the halo overdensity slice for one of our simulations at z=0.5, using halos with masses  $\log M_h \in [13.0, 13.5]$   $h^{-1}M_{\odot}$ .

As a second dataset to compute uncertainties on our measurements, we use a large ensemble of N-body simulations from the Quijote suite [144] with Gaussian initial conditions. Each Quijote simulation evolves dark matter particles in a periodic box of 1  $h^{-1}$ Gpc on a side, with resolutions ranging from 256<sup>3</sup> up to 1024<sup>3</sup> particles per box. High-resolution (HR) Quijote runs used in this work have the finest resolution and evolve  $1024^3$ particles. The simulations are run using the Gadget-2 code [145]. Snapshots are saved at multiple redshifts (z = 0, 0.5, 1, 2, 3), and we use z = 0, 0.5, 1, 2 in this work. The HR simulations correspond to an ensemble of 100 independent realizations and a fiducial cosmology consistent with Planck 2018 best-fit [117]. They share the same baseline cosmological parameters and volume, but have different initial random seeds.

## B. Extracting and fitting transfer functions

We use the field-level technique to measure the EFT parameters from our simulated halo catalogs. The fieldlevel methodology enables cosmic variance cancellation, allowing for precision measurements of EFT parameters from our simulations. To compute the best-fit field-level EFT models, we use the publicly available perturbative forward model code Hi-Fi mocks [29, 72, 93, 94, 110]. Hi-Fi mocks computes the optimal field-level bias transfer functions by minimizing the error between the simulated tracer density field and the EFT forward model. quantified by the error power spectrum (29). Comparing these transfer functions with the EFT computations allows one to determine the constant EFT parameters. In our implementation, the density and shifted fields are constructed on a regular Fourier grid with grid size  $N_{\rm mesh} = 512$  for the four N-body PNG simulations and  $N_{\rm mesh}=256$  for the Gaussian Quijote HR simulations, which correspond to Nyquist wavenumbers  $k_{\rm Nyq} \simeq 1.61\,h\,{\rm Mpc}^{-1}$  and  $0.80\,h\,{\rm Mpc}^{-1}$ , respectively. These are much larger than scales used in our analysis.

To propagate uncertainties in our measurement of  $\beta_X(k)$ ,  $X \in \{1, 2, \mathcal{G}_2\}$ , and compute error bars on our measured PNG bias  $b_{\psi}$ , we use the variance of  $\beta_X(k)$  across the Quijote HR ensemble to build the covariance matrix. Figure 2 shows the mean and spread of  $\beta_1(k)$  across these realizations for different halo mass bins at z = 0.5. For each mass bin, we compute the variance of  $\beta_X(k)$  at fixed k across the simulation ensemble to compute the covariance matrix for the transfer function. The diagonal elements of this matrix,  $\sigma_{\beta_X}^2(k)$ , are the effective scale-dependent errors on our measured  $\beta_X(k)$ . In our field-level fits using weighted least-squares,  $\sigma_{\beta_X}(k)$  then quantifies the uncertainty vector in the  $\chi^2$  minimization. Concretely, the function minimized by our weighted least-squares fits is the chi-square statistic writ-

ten in terms of the likelihood  $\mathcal{L}_{\beta_X}$  as

$$-2\ln \mathcal{L}_{\beta_X}(\theta) = \sum_{k} \frac{\left[\beta_X^{\text{data}}(k) - \beta_X^{\text{model}}(k;\theta)\right]^2}{\sigma_{\beta_X}^2(k)}, \quad (56)$$

which corresponds to a Gaussian likelihood. Here,  $\beta_X^{\text{data}}(k)$  is the transfer function measured from our PNG simulations,  $\beta_X^{\text{model}}(k)$  are our models, and  $\theta$  is the set of free bias parameters being fit. This way, our error bars on  $b_{\psi}$  capture the stochastic scatter of  $\beta_X(k)$  due to cosmic variance and shot noise.

As in [146], we use the following template to fit and extract the bias parameters  $b_2$ ,  $b_{\mathcal{G}_2}$  from  $\beta_2$ ,  $\beta_{\mathcal{G}_2}$ :

$$\beta_X^{\text{model}}(k; \{a_0^X, a_1^X, a_2^X\}) = a_0^X + a_1^X k^2 + a_2^X k^4, \quad (57)$$

for  $X = \{2, \mathcal{G}_2\}$ . Then we take  $a_0^X$  as a measurement of the corresponding bias parameter. We always fix  $b_2$  and  $b_{\mathcal{G}_2}$  to the transfer function best-fit values.

As for  $b_1, b_{\Gamma_3}, b_{\nabla^2 \delta}, b_{\psi}$ , we fit them from the shape of  $\beta_1(k)$  using eq. (50) in three different ways to get  $b_{\psi}$  measurements:

a. All parameters free. First, in our analysis, the simplest way to start is by fitting  $\theta = \{b_1, b_2, b_{\mathcal{G}_2}, b_{\Gamma_3}, b_{\nabla^2 \delta}, b_{\psi}\}$  to  $\beta_1^{\text{model}}(k) = \beta_1^{\text{NG}}(k)$  (eq. (50)).

However, since this leads to many free parameters with known degeneracies, it would be a good strategy to reduce the number of free parameters during our fits.

b. Fixing  $b_{\Gamma_3}, b_{\nabla^2 \delta}$  to their Gaussian values. One way to reduce the number of free bias parameters is to fix them to their best-fit Gaussian values extracted from the Gaussian control simulations. To that end we first fit  $\theta = \{b_{\Gamma_3}, b_{\nabla^2 \delta}\}$  to  $\beta_1^{\text{model}}(k) = \beta_1^{\text{G}}(k)$  (eq. (32)) and then use these values when fitting  $\theta = \{b_1, b_2, b_{\mathcal{G}_2}, b_{\psi}\}$  to  $\beta_1^{\text{model}}(k) = \beta_1^{\text{NG}}(k)$ .

The above approach, however, has an important limitation. The usual bias parameters of PNG simulations depend on  $f_{\rm NL}$ . In the context of simple analytic models like PBS, this follows from the rescaling of the peak height with  $f_{\rm NL}$  [46, 69, 140, 147].

$$\nu^* = \frac{\delta_c}{\sigma(M)} \left( 1 - \frac{\delta_c}{3} S_3(M) \right)^{1/2} , \qquad (58)$$

where  $\delta_c$  is the spherical collapse critical density,  $\sigma(M)$  is the mass variance of the initial density field in a spherical cell enclosing mass M, and  $S_3$  is the  $f_{\rm NL}$ -dependent skewness of the PDF of the initial density.

Let us present now a simple EFT-based argument that can be used to estimate this effect entirely within the effective description. In principle, the EFT expansion should include cubic terms like

$$\delta \big|_{\text{EFT,NG}}^{\text{n-pf}} \supset f_{\text{NL}} \psi \delta_1^2 \ .$$
 (59)

The contribution from this term is fully absorbed into  $b_1$  and  $b_{\psi}$  at halo power spectrum level to one-loop order.

Let us use the EFT naturalness arguments to estimate the typical shift of  $b_1$  due to this effect. We have

$$P_{13}^{\psi\delta_1^2} \supset 3b_1 f_{\rm NL} P_{11}(k) \int_{\mathbf{q}} P_{1\psi}(q) \equiv 2b_1 \Delta b_1 \big|_{\psi\delta_1^2} P_{11}(k) . \tag{60}$$

A direct evaluation in our fiducial cosmology at z=0.5 gives

$$\Delta b_1 \big|_{\psi \delta_1^2} \simeq \frac{3}{2} f_{\rm NL} \int_{q \le \Lambda} \frac{q^2 dq}{(2\pi)^3} \frac{q^2}{k_{\rm NL}^2} \frac{P_{11}(q)}{\mathcal{M}(q)}$$

$$\lesssim 0.1 \left(\frac{f_{\rm NL}}{10^3}\right) , \quad \text{for} \quad \Lambda = 0.7 \ h \text{Mpc}^{-1} .$$
(61)

One can obtain similar estimates for the shifts of the other bias parameters following the arguments on their renormalization at the level of the one-loop bispectrum [90]. While the renormalization of Gaussian bias parameters due to  $f_{\rm NL}$  is a very weak effect, its magnitude is comparable with the physical effect of the scale-dependent bias, and hence re-using the Gaussian values for these parameters may not be a good approximation. Therefore, this option is considered to be the most extreme in our list.

c. Using an empirical relation for  $b_{\Gamma_3}$ , with all other parameters free. In another approach to reduce the number of free parameters, we utilized a tight empirical relation between  $b_{\Gamma_3}$  and  $b_{\mathcal{G}_2}$  in order to fix  $b_{\Gamma_3}$  using our measured values of  $b_{\mathcal{G}_2}$ . This tight empirical relation has been noticed before in [29] in the context of galaxies. To validate it, we directly measure both  $b_{\mathcal{G}_2}$  and  $b_{\Gamma_3}$  in the Quijote HR Gaussian simulations. Figure 3 shows the resulting measurements at z=0.5, where each point corresponds to a halo mass bin in one of the 100 realizations. We see a tight correlation between  $b_{\Gamma_3}$  and  $b_{\mathcal{G}_2}$ , similar to the one found by  $[29]^3$ ,

$$b_{\Gamma_3} = -2.90 \, b_{\mathcal{G}_2} - 0.13 \,,$$

confirming that this empirical formula provides an accurate description of  $b_{\Gamma_3}$  across halo populations.

While this correlation has been derived in the context of the Gaussian simulations, is expected to hold even in PNG universes. The reason is that under the assumption of a universal mass function, at the leading approximation the PNG simply rescales the peak height without modifying the shape of the halo mass function [147]. Then it is easy to show that local halo bias parameters  $b_n$  in PNG Universes retain the same dependency on the (modified) peak height as in the Gaussian universe. This implies that correlations between local bias parameters do not depend on PNG in this approximation.

As far as the non-local bias parameters such as  $b_{\mathcal{G}_2}$  and  $b_{\Gamma_3}$  are concerned, empirically it was also found that they

<sup>&</sup>lt;sup>3</sup> Here we use a more conservative scale cut  $k_{\rm max}=0.2~h{\rm Mpc}^{-1}$  which leads to a relation slightly different from the one found in [29] at  $k_{\rm max}=0.4~h{\rm Mpc}^{-1}$ .

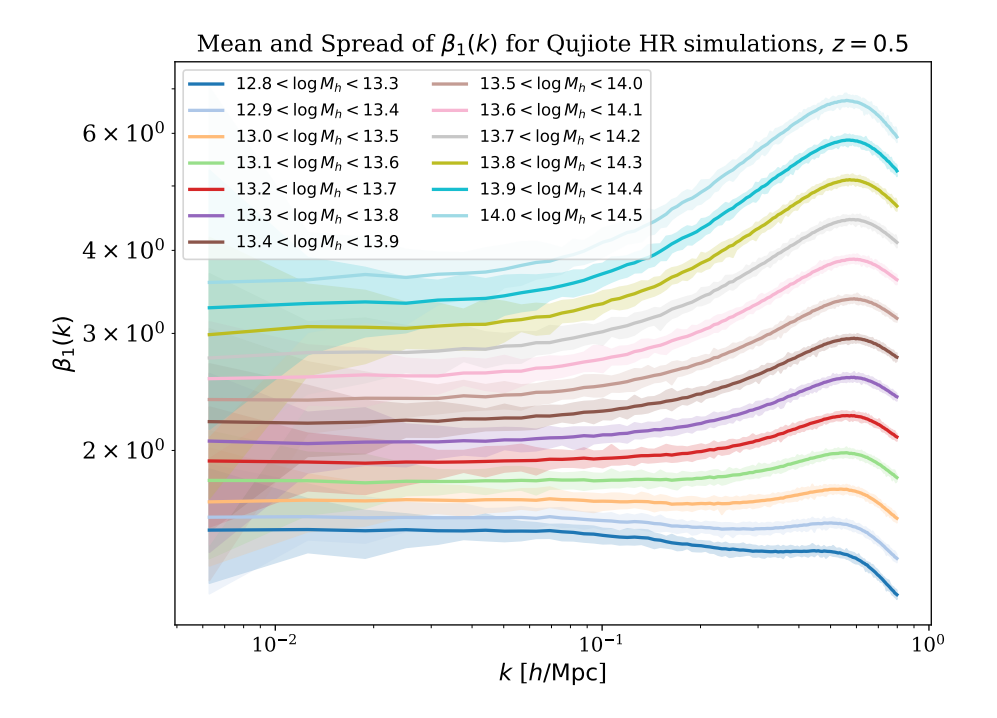


FIG. 2: Mean and spread of the halo–matter transfer function  $\beta_1(k)$  measured from the Gaussian Quijote HR simulations at z=0.5. Each solid curve shows the mean  $\beta_1(k)$  across 100 independent realizations for a given halo mass bin, in units of  $h^{-1}M_{\odot}$ , while the shaded region indicates the full range (minimum to maximum) across the ensemble. For a fixed mass bin, the transfer function is nearly scale-independent on large scales, but exhibits a strong upturn toward smaller scales ( $k \gtrsim 0.1 \, h \, \mathrm{Mpc^{-1}}$ ), with the amplitude increasing systematically with halo mass.

primarily depend on the peak height just as the local biases  $[72, 73]^4$ . Thus, it is natural to extend the above argument to these parameters as well. In other words, there is a generalized definition of the peak height in the PNG case that implies a degeneracy between  $f_{\rm NL}$  and the halo mass. This degeneracy is very similar to the degeneracy between the amplitude of mass fluctuations and the halo mass that can be used to explain the approximate cosmology and redshift-independence of the correlations between Gaussian halo bias parameters [35, 72, 73, 148].

While the above argument relies on certain simplifying assumptions and extrapolations, it suggests that one can treat the correlations between EFT parameters as approximately  $f_{\rm NL}$  independent. In agreement with this, we will see shortly that the actual Gaussian bias parameters  $b_2$  and  $b_{\mathcal{G}_2}$  as functions of  $b_1$  from the simulations do not appreciably depend on  $f_{\rm NL}$  for  $b_1\lesssim 4$ .

To sum up, as final fitting strategy, we use this relation to fix  $b_{\Gamma_3}$  when fitting  $\theta = \{b_1, b_2, b_{\mathcal{G}_2}, b_{\nabla^2 \delta}, b_{\psi}\}$  to  $\beta_1^{\text{model}}(k) = \beta_1^{\text{NG}}(k)$ .

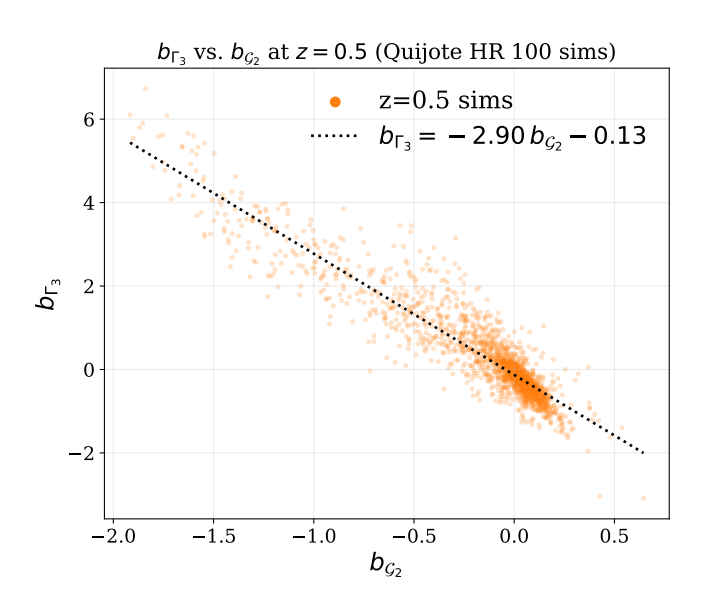


FIG. 3: Halo bias measurements of  $b_{\Gamma_3}$  versus  $b_{\mathcal{G}_2}$  from 100 Quijote HR simulations with Gaussian initial conditions at z=0.5. Each point corresponds to a fit for one simulation and halo mass bin. The black dotted line shows the empirical relation  $b_{\Gamma_3}=-2.90b_{\mathcal{G}_2}-0.13$ . The measurements closely follow the linear relation across the full range of  $b_{\mathcal{G}_2}$  values.

<sup>&</sup>lt;sup>4</sup> This simplified argument neglects the impact of the tidal field on the bias parameters through an ellipsoidal collapse barrier [35].

#### IV. RESULTS

In this Section, we present the results using our field-level methodology to measure  $b_{\psi}$ . We show that a field-level EFT forward model with scale-dependent transfer functions accurately reconstructs the simulated halo field, leaving only small-scale residuals (section IV A). Measuring the transfer functions shows a systematic PNG-induced offset relative to Gaussian initial conditions, allowing for a nonzero measurement of  $b_{\psi}$ . We make these measurements of  $b_{\psi}$  in section IV B using the three fitting strategies discussed in section III and extend our analysis to other redshifts in section IV C. We also compare our measurements against theoretical predictions from the PBS framework in section IV D, and find that  $b_{\psi}$  strengthens with halo mass and redshift, in qualitative agreement with PBS expectations.

## A. Overview of fields and transfer functions

In Figure 4 we show the field-level comparison, with and without PNG, between the simulated halo overdensity field and the best-fit forward model for z = 0.5 and halo masses  $\log M_h \in [13.0, 13.5] \ h^{-1} M_{\odot}$ . The left panels show slices of the simulated field, while the middle panels show the corresponding best-fit forward model. The slices shown here correspond to a finite slice depth of  $120 h^{-1}$ Mpc, and have been smoothed with a Gaussian kernel of width  $R = 4 h^{-1}$ Mpc in order to highlight the large-scale modes relevant to our EFT description. Visually, the prominent structures such as clusters, filaments, and voids are well matched between the fields. The similarity between the left and middle panels shows that the EFT expansion accurately reproduces the large scale features of the simulated field. This is true for simulations with PNG (top row) as well as Gaussian initial conditions (bottom row). Comparing the two simulation halo fields, we see that both exhibit the broad cosmic web features, but the PNG simulation shows more clustering around overdense regions, as expected because of the large  $f_{\rm NL}$ value used in our PNG simulations. The rightmost panel shows the residual field  $\delta_h^{\rm truth} - \delta_h^{\rm best-fit}$ , which is dominated by small-scale fluctuations that are not captured by our model. Overall, the forward model with the optimized transfer functions can accurately reconstruct the halo overdensity field.

To quantify how the halo overdensity field traces the underlying matter density field, we measure the EFT transfer functions, described in section II C, in simulations with Gaussian initial conditions as well as with PNG. These transfer functions encapsulate the scale dependence of the relation between halos and matter, and they are the key observables for distinguishing Gaussian from non-Gaussian initial conditions in our field-level approach. These measured transfer functions are shown in figure 5 for z = 0.5 and halo masses  $\log M_h \in [13.5, 14.0] h^{-1}M_{\odot}$ . The orange curves are measurements

from simulations with Gaussian initial conditions, while the blue curves are from simulations with equilateral PNG. The Gaussian transfer functions are roughly constant on large scales but show a scale dependence at smaller scales due to nonlinear bias effects. When equilateral PNG is introduced, the transfer functions are shifted relative to the Gaussian case. The magnitude of these shifts is consistent with our theoretical estimate from eq. (61).

We see that almost all of the measured transfer functions in the PNG simulations lie systematically below their Gaussian counterparts, with the exception of  $\beta_{\mathcal{G}_2}$ , showing that halos are less biased in our  $f_{\rm NL}=1000$  simulations. We observe a clear offset at all scales, consistent with the theoretical expectation [31] that equilateral PNG produces a scale-dependent modification to halo clustering that is more subtle than the case of local PNG, which induces a bias  $\propto k^{-2}$ . The clear offsets show that the field-level approach is sensitive to the PNG-induced bias differences.

The right panel of Fig. 5 also shows the error power spectrum of the field level model with respect to the simulated halos. In the leading approximation, the large-scale amplitude of the power spectrum is given by the Poisson expectation. PNG modulates the total number density of halos of a given mass (e.g. through the change in the mass variance) - more positive  $f_{\rm NL}$  generally leads to larger (high-mass) halos (see e.g. Fig. 1 of Ref. [149]). Since the linear bias of a higher number density sample of halos selected by mass is smaller, this is consistent with the reduction in  $b_1$  in the non-Gaussian simulations seen in the left panel of Fig. 5. Additional PNG-dependent changes in the scale dependence of  $P_{\rm err}$  are due e.g. to additional stochastic terms correlated with the potential (starting with  $\epsilon_{\psi}\psi$  [35]).

## B. Field-level bias measurements

The offset observed in the field-level transfer function  $\beta_1(k)$  between simulations with Gaussian initial conditions and PNG allows us to measure a nonzero value for the PNG bias parameter  $b_{\psi}$  by using eq. (50). The strength of the PNG bias signal in our field-level fits depends on the range of scales included, as well as the treatment of higher-order bias parameters. Higher-order bias terms, such as  $b_{\Gamma_3}$  and  $b_{\nabla^2 \delta}$  in eq. (32) absorb part of the small-scale dependence of  $\beta_1(k)$ . Since the fit results are sensitive to the amount of small-scale information we include as well as how we treat higher-order and higherderivative bias parameters, we present our results using three fitting strategies, each using three different values of  $k_{\rm max}$ , in this section and use the final strategy as a baseline for the remainder of the paper. All results shown in the rest of this paper are averaged over the four equilateral PNG simulations used in this work, described in section III.

First, we try fitting everything  $(b_1, b_{\psi})$  as well as the

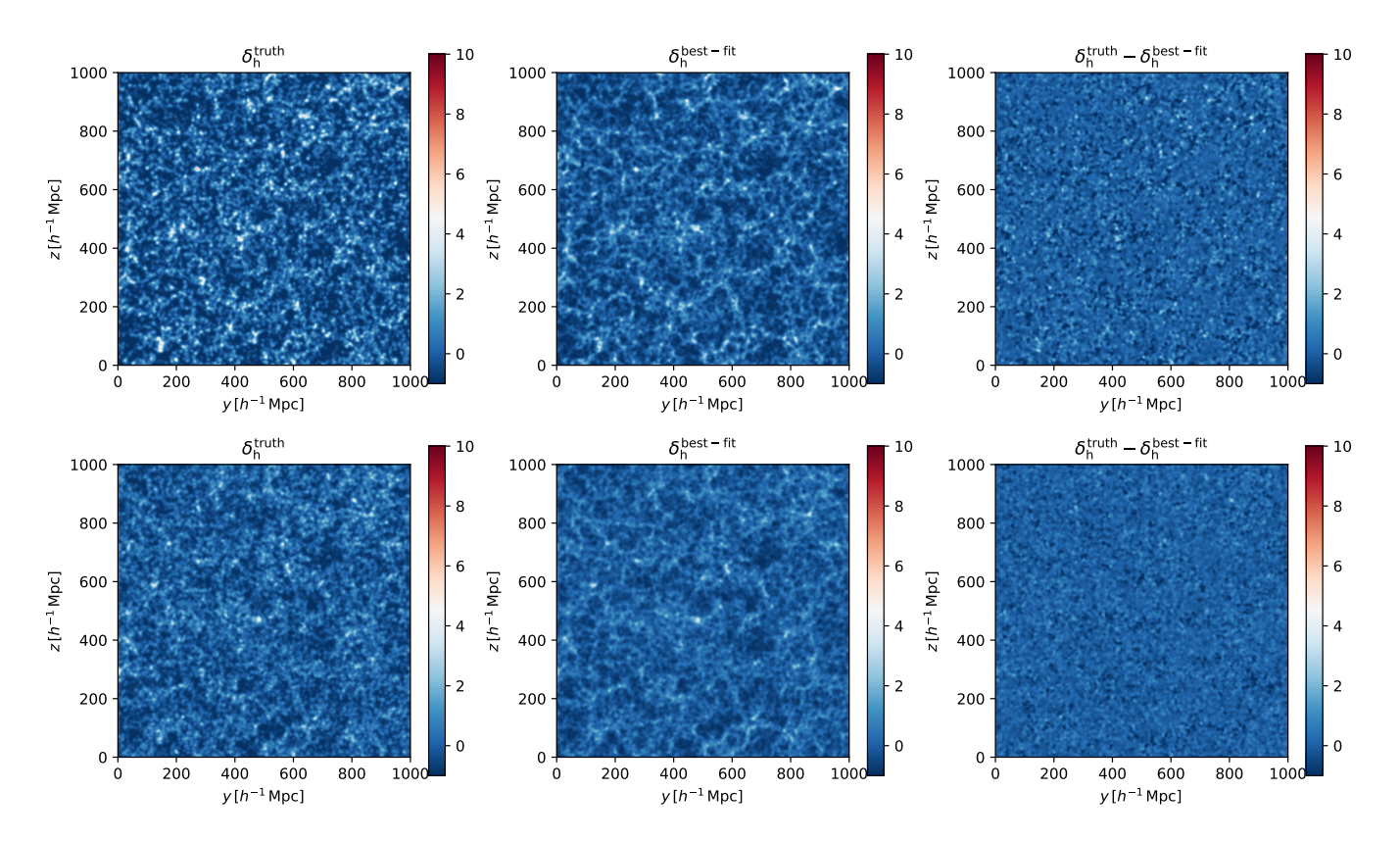


FIG. 4: Field-level comparison between the simulated halo overdensity field and the best-fit forward model for z=0.5 and halo masses  $\log M_h \in [13.0, 13.5] \ h^{-1}M_{\odot}$  computed using Hi-Fi mocks. The top row shows the comparison for a simulation with PNG, while the bottom row presents the corresponding comparison for the Gaussian (PNG-free) initial conditions. The left panel shows the simulated halo overdensity slice,  $\delta_h^{\rm truth}$ , taken directly from the simulation. The middle panel displays the corresponding best-fit forward-modeled field,  $\delta_h^{\rm best-fit}$ , computed by linearly combining the basis operators with the optimal transfer functions. The right panel shows the residual field,  $\delta_h^{\rm truth} - \delta_h^{\rm best-fit}$ , which quantifies the model error.

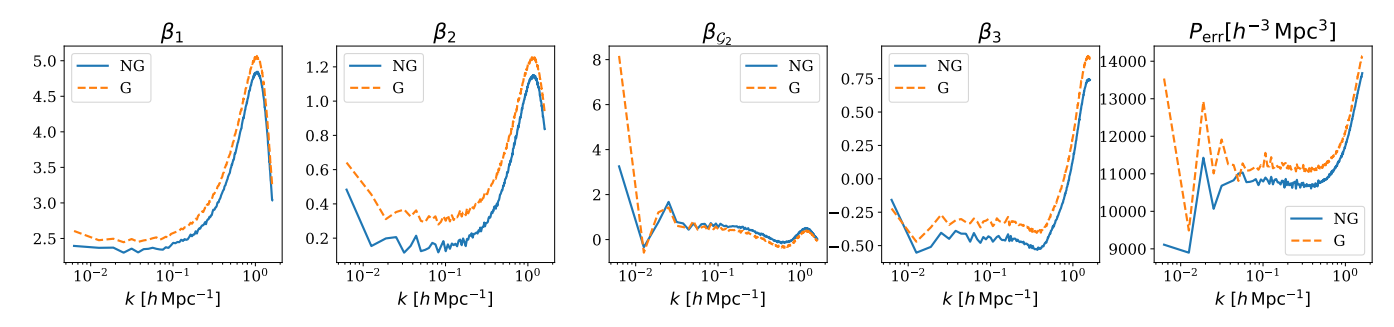


FIG. 5: Comparison of the field-level bias transfer functions  $\beta_1(k)$ ,  $\beta_2(k)$ ,  $\beta_{\mathcal{G}_2}(k)$ ,  $\beta_3(k)$ , along with the residual power spectrum,  $P_{\text{err}}(k) \equiv \left\langle \left| \delta_h^{\text{best-fit}}(\mathbf{k}) - \delta_h^{\text{truth}}(\mathbf{k}) \right|^2 \right\rangle'$ , for halo masses  $\log M_h \in [13.5, 14.0] \ h^{-1} M_{\odot}$  at redshift z = 0.5. Results are averaged across the four simulations and shown with (blue) and without (orange) PNG, measured using Hi-Fi mocks. The scale-dependent offset induced by equilateral PNG is visible in the PNG curve.

bias parameters  $b_{\Gamma_3}$  and  $b_{\nabla^2 \delta}$ ) to the transfer functions obtained from the PNG simulations using eq. (50). Our measured  $b_{\psi}$  values as a function of halo mass for z=0.5 are shown in the left panel of Figure 6. The three curves correspond to fits with increasing  $k_{\rm max}$  values, to show how the inferred  $b_{\psi}$  value changes as more small-scale

information is included. To study the sensitivity of our model to  $b_{\psi}$  at the field level, we show the difference in  $\chi^2$  statistic between our fits with and without  $b_{\psi}$ ,  $\Delta \chi^2 = \chi^2(b_{\psi} \neq 0) - \chi^2(b_{\psi} = 0)$ , in right panel of Figure 6. Overall, we can see that including more small scale information increases our sensitivity to the PNG-induced

bias. However, the fits are consistent with  $b_{\psi}\approx 0$  for all values of  $k_{\rm max}$ . This is reflected in  $\Delta\chi^2$  curves in the right panel, where we do not see a statistically significant detection of nonzero  $b_{\psi}$  for any curve. When both  $b_{\Gamma_3}$  and  $b_{\nabla^2\delta}$  are free, essentially all of the  $b_{\psi}$  signal is washed out. This shows that  $b_{\psi}$  is degenerate with these parameters - for instance,  $b_{\nabla^2\delta}$  captures the  $k^2$  part of the PNG-induced scale dependence [35, 119]. As a result, the fits remain consistent with  $b_{\psi}\approx 0$  for all  $k_{\rm max}$  values, and  $\Delta\chi^2$  is not significant.

To get a nonzero measurement of  $b_{\psi}$  by breaking this degeneracy and reducing the number of free parameters, we next fix  $b_{\Gamma_3}$  and  $b_{\nabla^2\delta}$  to their values measured from Gaussian simulations (using eq. 32), leaving only  $b_1$  and  $b_{\psi}$  free in the fits to  $\beta_1$ . Figure 7 shows our results using this fitting strategy. This fitting strategy pins down  $b_{\psi}$  more tightly, and the sensitivity increases with higher  $k_{\text{max}}$ . However, because  $b_{\nabla^2 \delta}$  lies along a strong degeneracy direction with  $b_{\psi}$ , fixing it to the Gaussian value forces the fit to compensate by changing  $b_{\psi}$  and makes the fits sensitive to the  $k_{\rm max}$  used. In the left panel, we see that the inferred trend in  $b_{\psi}$  is sensitive to the choice of  $k_{\text{max}}$ . At low  $k_{\text{max}}$ , the fits prefer stronger mass dependence and significant negative values at high mass. At high  $k_{\rm max}$ , the fitted  $b_{\psi}$  is nearly flat and close to 0, with smaller uncertainties compared to the lower  $k_{\text{max}}$ fits. Thus, this fitting strategy leads to biased and inconsistent estimates of  $b_{\psi}$ , which can also be observed in the  $\Delta \chi^2$  curves as a function of  $k_{\text{max}}$ ; the fits do not behave coherently, indicating that the model is mis-specified.

Given the strong degeneracy between  $b_{\nabla^2\delta}$  and  $b_{\psi}$ , we know that  $b_{\nabla^2\delta}$  should not be fixed in order to get robust measurements. Instead, we can try to fix only  $b_{\Gamma_3}$ . So, in the third approach to reduce the number of free parameters while robustly measuring  $b_{\psi}$ , we used an empirical linear fit between  $b_{\Gamma_3}$  and  $b_{\mathcal{G}_2}$  similar to the one measured across 10,500 BOSS-like HOD galaxy mocks with a field-level EFT pipeline in [29]:  $b_{\Gamma_3} = -2.90 \, b_{\mathcal{G}_2} - 0.13$ .

In Figure 8 we show our fit values of  $b_{\psi}$  when fixing  $b_{\Gamma_3}$  using this relation and fitting  $b_1, b_{\nabla^2 \delta}, b_{\psi}$ . The resulting  $b_{\psi}$  measurements are stable across  $k_{\text{max}}$  values, and we see a weak detection at large scales, and increasingly nonzero  $b_{\psi}$  as more small-scale information is included. At the lowest cutoff  $k_{\text{max}} = 0.107 \ h/\text{Mpc}$ , the fitted  $b_{\psi}$ values are relatively small in magnitude, especially for low-mass halos. For the lowest mass halos, the fit is consistent with  $b_{\psi} \approx 0$  using this  $k_{\text{max}}$ . For the more massive halos, however, we measure a non-zero  $b_{\psi}$  at this cutoff scale. This is reflected in  $\Delta \chi^2$  curve for  $k_{\rm max} = 0.107$  in the right panel, which dips below zero at high masses. At this large-scale cut, a non-zero PNG bias is only weakly preferred except in the case of very biased tracers. This is expected because equilateral PNG induces only a weak scale-dependent effect on large scales, so we need very biased halos to notice such small enhancements. As we extend to smaller scales, however, the measured  $b_{\psi}$  values become non-zero for most mass bins, and the error bars shrink. The improvement in fit sensitivity is correspondingly large: the right panel shows  $\Delta \chi^2 < 0$  for essentially all masses using higher  $k_{\rm max}$ .

As an additional test, we apply this fitting strategy to the Gaussian simulations, and find that our measurements of  $b_{\psi}$  are consistent with zero within  $2\sigma$  for all halo masses. This test is described in Appendix A.

For the remainder of the paper, we use the strategy based on the empirical  $b_{\mathcal{G}_2} - b_{\Gamma_3}$  relation as our baseline when fitting for  $b_{\psi}$ .

To study the impact of PNG on the relations among bias parameters, we show the  $b_2-b_1$  and  $b_{\mathcal{G}_2}-b_1$  trends for all halo mass bins and redshifts, with points colored by redshift, in Figure 9. The tight correlations indicate that both  $b_2$  and  $b_{\mathcal{G}_2}$  are well described as functions of  $b_1$ . Importantly, these relations are not significantly modified with PNG, as can be seen from the similar trends that the Gaussian and non-Gaussian samples follow across redshifts. This suggests the validity of our use of Gaussian relations between bias parameters to break degeneracies when fitting  $b_{\psi}$  from PNG simulations.

## C. Redshift dependence

In Figure 10, we present a comparison of the field-level fits of  $b_{\psi}$  at multiple redshifts as a function of the linear bias  $b_1$ , which is an increasing, monotonic function of halo mass. Hence, each successive point for a given redshift corresponds to an increasing halo mass bin with  $\log_{10}(M/h^{-1}M_{\odot}) \in [12.0, 12.5], [12.1, 12.6], \ldots, [14.0, 14.5]$ . We obtain our  $b_{\psi}$  values using our baseline fitting strategy with a  $k_{\text{max}} = 0.2 \ h\text{Mpc}^{-1}$ .

We expect that halos with larger  $b_1$  (i.e. rarer, more massive or higher redshift halos) should show stronger PNG response in  $b_{\psi}$ . This is precisely what we see in the figure. At low values of  $b_1$ ,  $b_{\psi}$  is indeed close to 0. Moreover, the fits reveal a coherent negative trend of  $b_{\psi}$  with increasing halo mass. The effect is weak at low masses but grows in amplitude for higher-mass halos, with the steepest decline at higher redshifts. This is qualitatively consistent with the expectation that rarer, more biased halos show the strongest response to PNG-induced mode coupling.

Looking across redshifts, we also find a consistent picture of redshift evolution of  $b_{\psi}$ . At z=0.0, the signal is weak, with  $b_{\psi}$  values clustering near zero. By z=1.0, a negative trend becomes more apparent, with amplitudes reaching  $\approx$  -2000 for the most massive bins. At z=2.0,  $b_{\psi}$  values plunge to  $\approx$  -5000 at high mass. These redshift trends are consistent with the growth of halo bias at early times as halos become rarer.

Figure 10 offers another consistency check. Notably, measurements from all four redshifts (z = 0, 0.5, 1.0, 2.0) fall along the same trend, hence we reproduce similar values of  $b_{\psi}$  for similar values of  $b_1$  across different mass ranges and cosmic epochs. To quantify this trend, we performed a global fit to all the measured values of  $b_{\psi}$ 

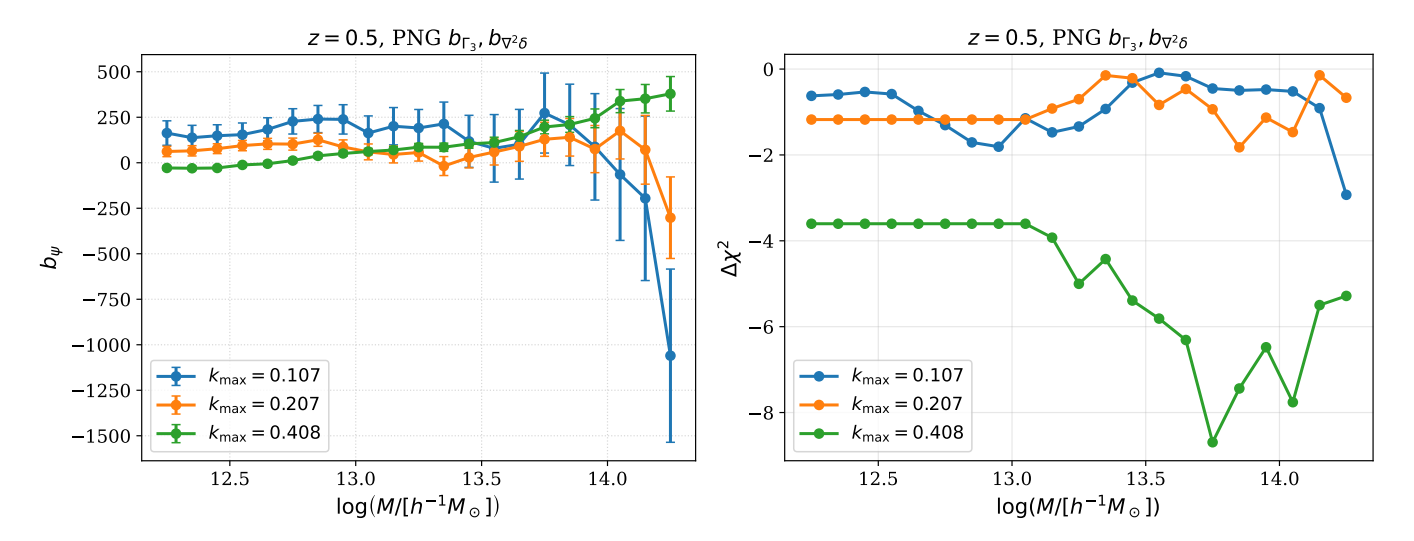


FIG. 6: Left Panel: Field-level fit values of PNG-induced bias parameter  $b_{\psi}$  from our non-Gaussian simulations as a function of halo mass for z=0.5. Here, we fit  $b_1, b_{\psi}, b_{\Gamma_3}$  and  $b_{\nabla^2 \delta}$  using  $\beta_1$  from simulations with PNG using eq. (50). The curves correspond to different  $k_{\text{max}}$  used in fitting. Right Panel: Detectability of  $b_{\psi}$  as a function of halo mass, measured using the difference in chi-squared statistic  $\Delta \chi^2 = \chi^2(b_{\psi} \neq 0) - \chi^2(b_{\psi} = 0)$ . Increasing  $k_{\text{max}}$  increases the sensitivity to  $b_{\psi}$  in all mass bins. For mass bins with  $\log M_h \lesssim 12.8 \, h^{-1} M_{\odot}$ , the number of halos in the Quijote ROCKSTAR suite is not converged. To avoid unreliable noise estimates, we assign these bins a conservative covariance as measured in the first converged bin,  $\log M_h \in [12.8, 13.3] \, h^{-1} M_{\odot}$ . This results in the nearly constant  $\Delta \chi^2$  plateau visible at low masses.

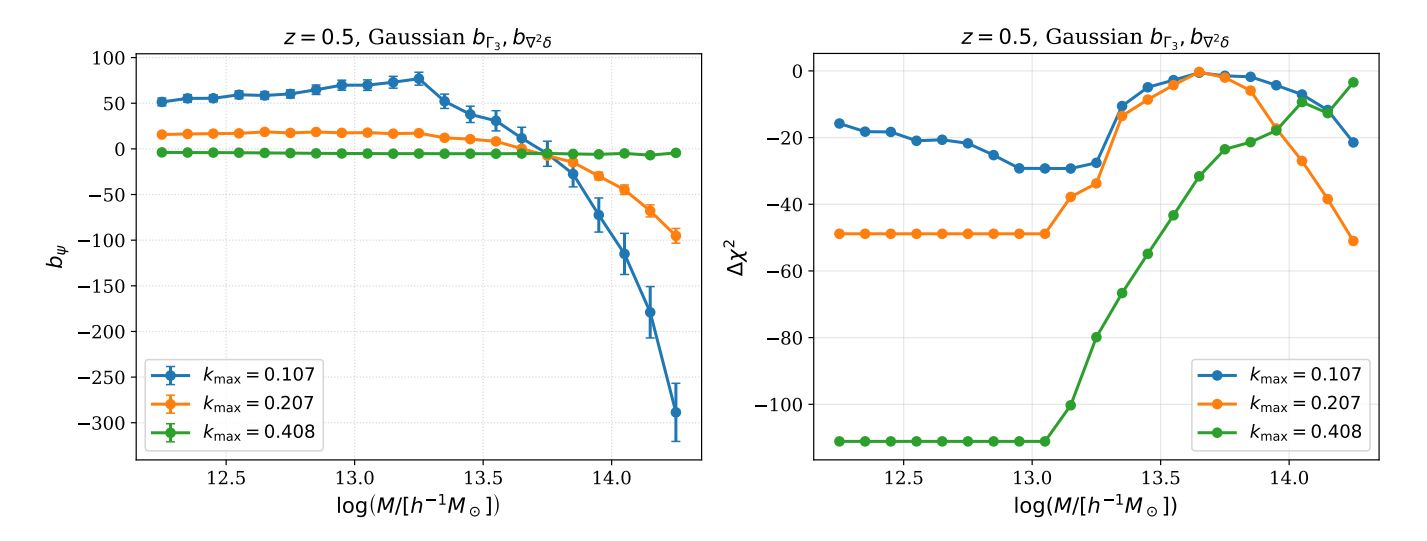


FIG. 7: Same as Fig. 6, but here we fix  $b_{\Gamma_3}$  and  $b_{\nabla^2 \delta}$  from Gaussian simulations using eq. 32 when performing our fit. As in Fig. 6, the  $\Delta \chi^2$  plateau at low masses is due to our conservative choice of a fixed constant covariance for these low mass bins.

across redshifts and mass bins using a simple quadratic relation, finding

$$b_{\psi} = -221 + 478b_1 - 152b_1^2. \tag{62}$$

The resulting fit is shown as the black dotted curve in Figure 10 and provides a compact description of our measurements, capturing both the overall negative scaling of  $b_{\psi}$  with  $b_1$  and the increasing magnitude of this effect for highly biased halos.

Finally, let us note that the above relation can be rewritten as a dependence of  $b_{\psi}$  on the generalized  $f_{\rm NL}$ -dependent peak height, which will display its implicit  $f_{\rm NL}$  dependence. However, since this dependence can be fully absorbed into  $b_1$ , the final prior is expected to be  $f_{\rm NL}$ -independent to a first approximation, which will be adequate for experimentally relevant values  $f_{\rm NL} \lesssim 300$  [29].

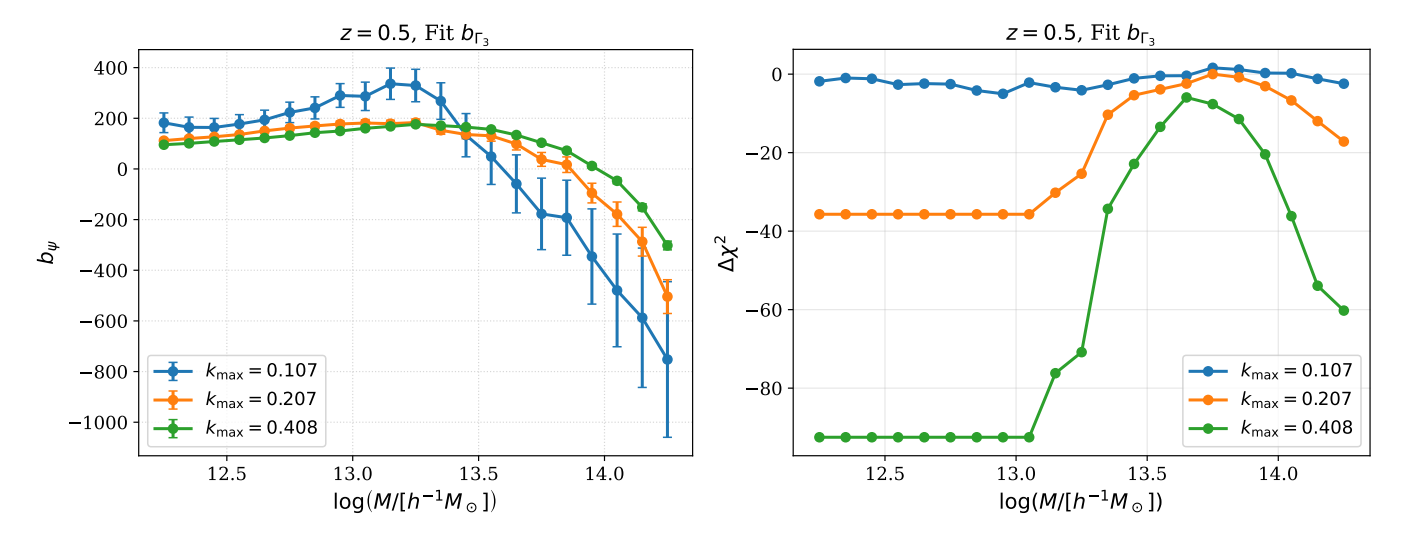


FIG. 8: Same as Fig. 7, but we use an empirical relation  $b_{\Gamma_3} = -2.90 \, b_{\mathcal{G}_2} - 0.13$  as in [29] and fit  $b_1, b_{\psi}, b_{\nabla^2 \delta}$  from  $\beta_1$ .

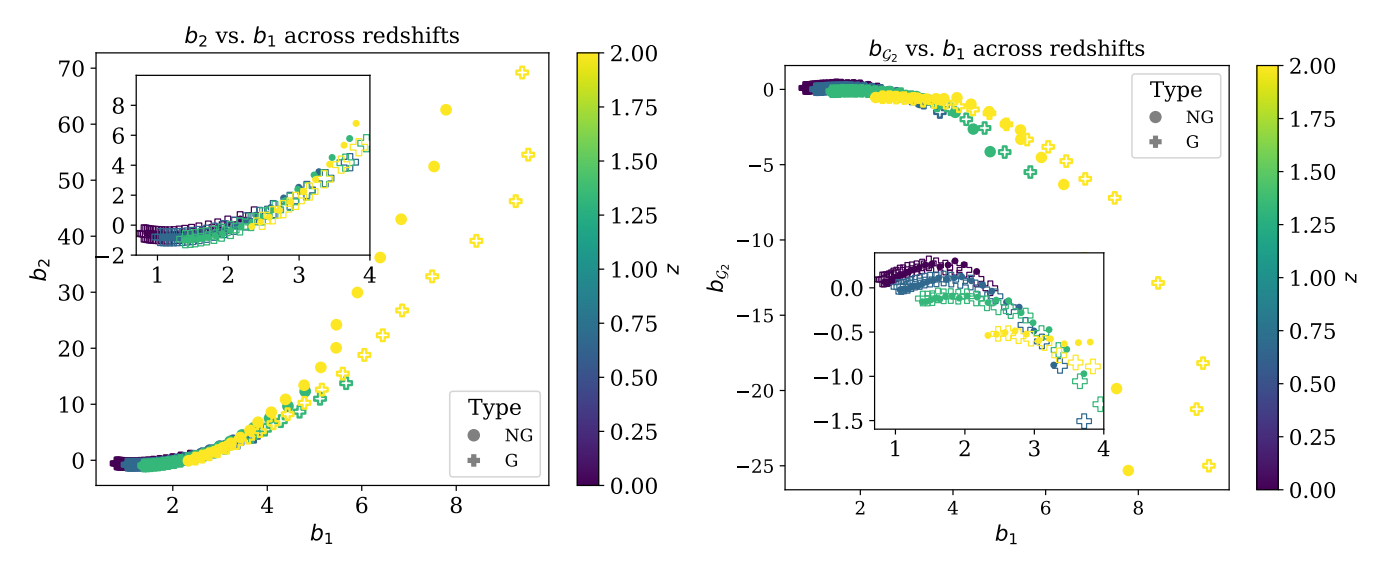


FIG. 9: Relations between higher-order halo bias parameters and the linear bias  $b_1$  across all redshifts and mass bins for both Gaussian (G, pluses) and non-Gaussian (NG, circles) simulations. **Left Panel:** quadratic bias  $b_2$  versus  $b_1$ , **Right Panel:** tidal bias  $b_{\mathcal{G}_2}$  versus  $b_1$ . The color scales encode redshift for  $z \in [0.0, 0.5, 1.0, 2.0]$ . The Gaussian and PNG values follow nearly identical trends, with pluses mostly overlapping with the circles, indicating that PNG does not significantly alter the relationships among the bias parameters.

# $\begin{array}{ccc} \textbf{D.} & \textbf{Comparison with Peak-Background Split} \\ & \textbf{Predictions} \end{array}$

Let us compare our measurements now with the predictions of the phenomenological peak-background split model (PBS).

The predictions from PBS cannot be directly compared against our measurements because of their cutoff dependence. In general, the EFT bias parameters are scheme and scale-dependent, and thus their measured values depend on the cutoff scale used within a given framework. A physically measurable quantity is the halo-matter cross power spectrum. Hence, this must be independent of the

cutoff scales and can be used to relate measurements from different frameworks.

The leading PNG one-loop halo-matter cross spectrum is given by

$$P_{hm} \supset b_1 P_{11} + f_{\text{NL}} b_{\psi} \frac{(k/k_{\text{NL}})^2}{\mathcal{M}(k)} P_{11} + P_{hm,12}(k), \quad (63)$$

where  $P_{hm,12}$  is given in eq. (51). In the UV limit  $k \ll p$ , the leading term from  $P_{hm,12}$  is the one proportional to

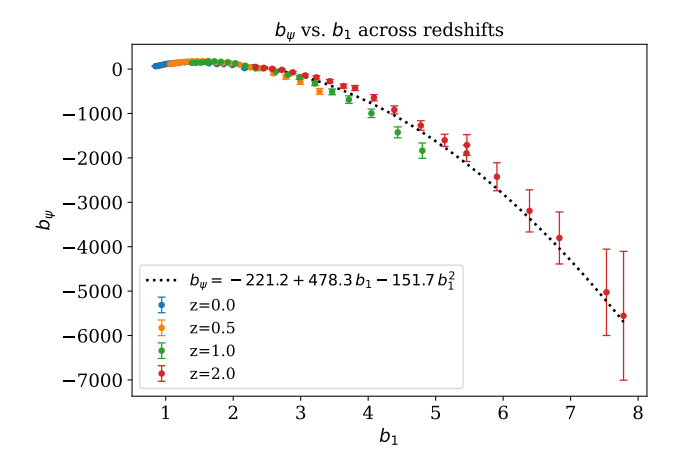


FIG. 10: Our measured  $b_{\psi}$  values versus the linear bias  $b_1$  across multiple redshifts. Each point for a given redshift corresponds to  $\log_{10}(M/h^{-1}M_{\odot}) \in [12.0, 12.5], [12.1, 12.6], \ldots, [14.0, 14.5]$ . Different colors correspond to the different redshifts used in this work. We see agreement with the PBS expectation that the magnitude of  $b_{\psi}$  grows with halo bias.

 $b_2$ ,

$$P_{hm,12}^{b_2} = \int_{\mathbf{p}} \frac{b_2}{2} B_{111}(k, p, |\mathbf{k} - \mathbf{p}|)$$

$$= \frac{b_2}{2} \mathcal{M}(k) \int_{\mathbf{p}} \mathcal{M}(p) \mathcal{M}(|\mathbf{k} - \mathbf{p}|) b_{\psi}(k, p, |\mathbf{k} - \mathbf{p}|).$$
(64)

Now, we can compute the UV limit of this term using the squeezed limit of the primordial bispectrum from eq. (9),

$$P_{hm,12}^{b_2} = 6b_2 k^2 \mathcal{M}(k) P_{\phi}(k) f_{NL} \times \int_{\mathbf{p}} \mathcal{M}^2(p) P_{\phi}(p) \frac{1 - (\hat{\mathbf{k}} \cdot \hat{\mathbf{p}})^2}{p^2} .$$
 (65)

Using  $\Lambda$  as the cutoff in the momentum integral, doing the angular integral, and using the linear matter power spectrum  $P_{11}(p) = \mathcal{M}^2(p)P_{\phi}(p)$ , we get

$$P_{hm,12}^{b_2}(k) = 12b_2 \, \frac{k^2}{\mathcal{M}(k)} \, P_{11}(k) \, f_{\rm NL} \, \int_0^{\Lambda} \frac{dp}{6\pi^2} \, P_{11}(p) \,, \tag{66}$$

implying the total cross-spectrum contribution

$$P_{hm}(k) \supset b_1 P_{11}(k) + f_{NL} \frac{(k/k_{NL})^2}{\mathcal{M}(k)} P_{11}(k) \times \left[ b_{\psi}(\Lambda) + 12b_2 k_{NL}^2 \int_0^{\Lambda} \frac{dp}{6\pi^2} P_{11}(p) \right]. \quad (67)$$

When we measure the PNG effects on the halo distribution, we effectively probe the scale-dependent second

term in the above equation. This measurable must be independent of the cutoff scale, for a given redshift z, and so we get the following Renormalization Group (RG) equation:

$$12b_2\sigma_v^2(\Lambda, z)k_{\rm NL}^2 + b_{\psi}(\Lambda) = 12b_2\sigma_v^2(\Lambda', z)k_{\rm NL}^2 + b_{\psi}(\Lambda'),$$
(68)

where we have defined

$$\sigma_v^2(\Lambda, z) = D^2(z) \int_0^{\Lambda} \frac{dp}{6\pi^2} P_{11}(p).$$
 (69)

The PBS predictions correspond to the limit of  $k \to 0$ ,  $\Lambda \to 0$  [35], while our field-level measurements correspond to  $\Lambda \to \infty$ , which matches the scheme used in CLASS-PT and data analysis e.g. [150]. Since  $\sigma_v^2(0,z) = 0$ , we have the following relation between our measurements,  $b_{\psi}(z)$ , and PBS predictions,  $b_{\psi}(\Lambda = 0, z)$ ,

$$b_{\psi}(\Lambda = 0, z) = b_{\psi}(z) + 12 b_2(z) \sigma_v^2(\Lambda \to \infty, z) k_{\text{NL}}^2$$
. (70)

This is the prediction appropriate for a comparison to PBS.<sup>5</sup> To evaluate  $b_{\psi}(\Lambda = 0, z)$  in practice, we use  $b_2$  extracted from the  $\beta_2$  fits.

We now compare our field-level measurement of the PNG bias to theoretical predictions from the PBS formalism. In figure 11, we compare our field-level measurement of  $b_{\psi}$  as a function of halo mass and redshift against the theoretical predictions derived from the equilateral PNG model in [31] for the baseline scale cut of  $k_{\text{max}} = 0.2h\,\text{Mpc}^{-1}$ . The solid lines show the theoretical predictions for  $b_{\psi}$  computed using their expression<sup>6</sup> for the correction to the Lagrangian bias,  $b_L$ , induced by equilateral PNG,

$$b_{\psi} = 6 b_L \, \delta_c \, \frac{\sigma_{R,-2}^2}{\sigma_R^2} k_{\rm NL}^2,$$
 (71)

where  $\delta_c = 1.686$  is the critical overdensity for spherical collapse, and  $\sigma_{R,n}$  are defined using the standard window  $W_R(k)$  as

$$\sigma_{R,n}^2 \equiv \int \frac{d^3k}{(2\pi)^3} \, k^n \, P_{11}(k) \, W_R^2(k). \tag{72}$$

For a real-space top-hat of radius R, the Fourier-space window is

$$W_R(k) \equiv 3 \frac{\sin(kR) - kR\cos(kR)}{(kR)^3},\tag{73}$$

<sup>&</sup>lt;sup>5</sup> A potential source of discrepancy between PBS and EFT could be RG effects of redundant cubic operators such as  $\psi \delta_1^2$ ,  $\psi \mathcal{G}_2$ . Their contribution is set to zero in the scheme used in CLASS-PT, which might generate additional corrections in the  $\Lambda \to 0$  limit required by the PBS. We leave this for future work.

<sup>&</sup>lt;sup>6</sup> In [31], the PNG correction is written as a scale-dependent shift to the Lagrangian bias,  $\Delta b_L^{\rm eq}(k) \propto b_L \delta_c \, k^2 \mathcal{M}^{-1}(k) \sigma_{R,-2}^2/\sigma_R^2$ . In our framework, this correction is equivalent to introducing the operator  $\psi(\mathbf{k}) \equiv k^2 \phi(\mathbf{k})$  with amplitude  $b_{\psi}$ . We therefore adopt  $b_{\psi}$  as our parameterization, with Eq. (71) giving the PBS prediction for its value.

where R corresponds to the Lagrangian radius of halos.

Eq. (71) encapsulates a few important scalings. First, the PNG bias contribution is proportional to the Gaussian bias  $b_L$  and hence grows for more massive halos. Second, it depends on redshift through  $b_L$  and variance  $\sigma_{R,n}$ , becoming larger at higher redshift for a fixed halo mass. These scalings are clearly visible in the solid lines of Figure 11.

The dotted lines in the figure show our measurements of  $|b_{\psi}|$  using the RG-corrected field-level measurements of the halo-matter linear transfer function  $\beta_1(k)$ . In both cases, we find that  $|b_{\psi}|$  increases with both halo mass and redshift. Qualitatively, we find agreement with the expectation that the bias induced by PNG is enhanced at high masses and redshifts, reflecting the growth of the Lagrangian bias parameter in the Press-Schechter framework [73, 151]  $b_L \propto \frac{\nu^2 - 1}{\delta_c}$ , with  $\nu = \frac{\delta_c}{\sigma(M,z)}$ . Quantitatively, we observe a tension between our measurements and the PBS model predictions. This is not very surprising given that the PBS model does not capture the complete physics of halo biasing, e.g. it does not account for tidal interactions. The quantitative mismatch between EFT measurements and PBS predictions highlights the limits of empirical structure formation models. whose accuracy will likely be insufficient for upcoming high precision galaxy surveys.

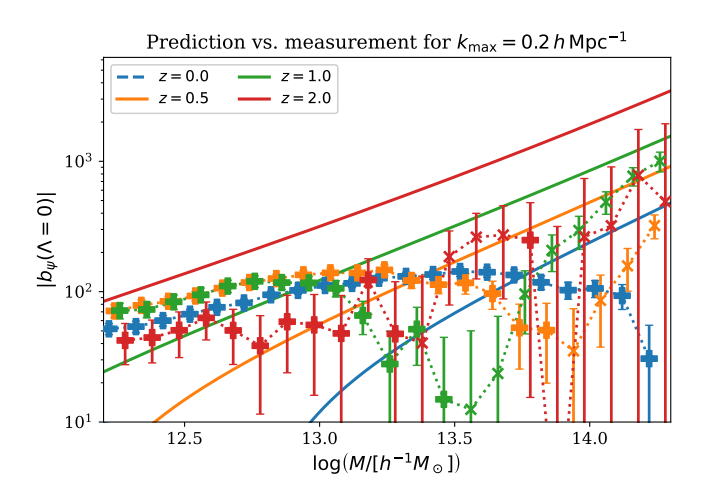


FIG. 11: Prediction for  $b_{\psi}$  as a function of halo mass and redshift from the PBS model (solid curves) [31] along with our measurements (dotted curves) run to  $\Lambda=0$  using the renormalization group flow (70). The marker shape encodes the sign of  $b_{\psi}$ , with plus symbols corresponding to positive values and crosses to negative values. Across all redshifts, the bias grows with increasing halo mass, and the magnitude of the bias is larger at higher redshifts, in agreement with baseline theoretical expectations.

#### V. CONCLUSIONS

We have studied the leading order scale-dependent halo bias due to equilateral primordial non-Gaussianity from N-body simulations. To that end we used the field-level EFT technique which allowed for a reduction of sampling noise in our measurements. Using an empirical relationship between the cubic and quadratic tidal biases suggested by N-body simulations, we were able to measure the equilateral PNG bias across various halo masses and redshifts.

Our work provides the first reliable estimates of the equilateral PNG bias parameters, which can be used to set priors in equilateral PNG analyses of galaxy clustering data, e.g. from the power spectra and bispectra of the DESI data [152]. Conservatively, one could use our measurements to set the width of the priors on this parameter to marginalize over. Alternatively, one could use our measurements to compute the analytic informative priors along the lines of [73], which might lead to better constraints on equilateral PNG.

Going forward, it will be interesting to extend our approach to the halo occupation distribution catalogs as in [29] and full hydrodynamical simulations [110]. It will also be interesting to study the higher-order equilateral PNG biases like  $b_{\psi\delta}$ . The corrections from these operators are suppressed in the power-counting relative to  $P_{12}$ , but they become important at the two loop order. Another obvious extension of our work is a detailed analysis of the other types of PNG: orthogonal non-Gaussianity and cosmological collider shapes [111, 153–165].

From the methodological point of view, it will be important to improve the field-level EFT in order to break the degeneracy between  $b_{\Gamma_3}$  and  $b_{\psi}$ . One way forward would be to include cubic operators like  $\Gamma_3$  explicitly in the field-level forward model. This will allow us to explicitly validate the assumption of the  $b_{\mathcal{G}_2} - b_{\Gamma_3}$  correlation and in principle, go beyond it. Additionally, it will be interesting to develop a consistent renormalization group treatment of the equilateral PNG parameters that would clarify their relationship with EFT loop computation schemes and redundant operators. We leave these research directions for future investigation.

### ACKNOWLEDGMENTS

MI thanks Oliver Philcox for useful discussions. KA acknowledges supports from Fostering Joint International Research (B) under Contract No.21KK0050 and the Japan Society for the Promotion of Science (JSPS)

 $<sup>^{7}</sup>$   $\psi\delta$  become important only at high orders because the equilateral PNG bispectrum is suppressed in the squeezed limit. This can be contrasted with the local PNG, where contributions from the  $\phi\delta$  operator have the same scaling as  $P_{12}$ , so it contributes already at the one loop.

KAKENHI Grant No.JP24K17056. Part of the numerical computations were carried out on Cray XD2000 system at Center for Computational Astrophysics, National Astronomical Observatory of Japan. JMS acknowledges that support for this work was provided by The Brinson Foundation through a Brinson Prize.

## Appendix A: Validation of the fitting prescription on Gaussian simulations

To validate our fitting strategy and ensure that the extracted PNG bias are not contaminated by numerical artifacts or fitting degeneracies, we apply the full analysis pipeline to a Gaussian simulation in which  $f_{\rm NL}=0$ . In this case,  $b_{\psi}=0$  at all masses. Figure 12 shows our recovered  $b_{\psi}$  values as a function of halo mass at z=0.5. For this fit we used  $P_{12}=0$  and set  $f_{\rm NL}=10^3$  to match the main PNG analysis. The fitted values are consistent with zero within the statistical uncertainties and show no systematic dependence on mass. The figure demonstrates that our fitting procedure is unbiased and robust when applied to Gaussian initial conditions, providing confidence that the non-zero  $b_{\psi}$  values observed in the PNG simulations truly arise from non-Gaussianity within the simulations rather than from the fitting procedure itself.

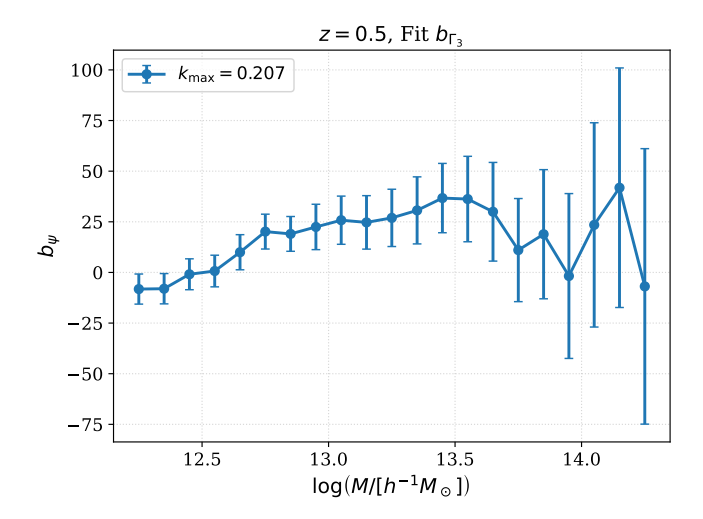


FIG. 12: Null test of our baseline  $b_{\psi}$  fitting procudure on Gaussian simulations at z=0.5. The fitted values of  $b_{\psi}$  are obtained by applying the same fitting pipeline used for the PNG simulations to a purely Gaussian realization, where the true  $b_{\psi}=0$ . The recovered values are consistent with  $b_{\psi}=0$ , with no systematic trend across halo mass, confirming that our fitting methodology does not introduce spurious PNG bias contributions.

- [1] DESI collaboration, The DESI Experiment Part I: Science, Targeting, and Survey Design, 1611.00036.
- [2] EUCLID collaboration, Euclid Definition Study Report, 1110.3193.
- [3] LSST collaboration, LSST: from Science Drivers to Reference Design and Anticipated Data Products, Astrophys. J. 873 (2019) 111 [0805.2366].
- [4] R. Akeson et al., The Wide Field Infrared Survey Telescope: 100 Hubbles for the 2020s, 1902.05569.
- [5] D. Babich, P. Creminelli and M. Zaldarriaga, The Shape of non-Gaussianities, JCAP 08 (2004) 009 [astro-ph/0405356].
- [6] N. Dalal, O. Dore, D. Huterer and A. Shirokov, The imprints of primordial non-gaussianities on large-scale structure: scale dependent bias and abundance of virialized objects, Phys. Rev. D 77 (2008) 123514 [0710.4560].
- [7] A. Slosar, C. Hirata, U. Seljak, S. Ho and N. Padmanabhan, Constraints on local primordial non-Gaussianity from large scale structure, J. Cosmology Astropart. Phys. 2008 (2008) 031 [0805.3580].
- [8] E.-M. Mueller, M. Rezaie, W. J. Percival, A. J. Ross, R. Ruggeri, H.-J. Seo et al., The clustering of galaxies in the completed SDSS-IV extended Baryon Oscillation Spectroscopic Survey: Primordial non-Gaussianity in Fourier Space, arXiv e-prints (2021) arXiv:2106.13725 [2106.13725].
- [9] E. Castorina, N. Hand, U. Seljak, F. Beutler, C.-H. Chuang, C. Zhao et al., Redshift-weighted constraints on primordial non-Gaussianity from the clustering of the eBOSS DR14 quasars in Fourier space, J. Cosmology Astropart. Phys. 2019 (2019) 010 [1904.08859].
- [10] B. Leistedt, H. V. Peiris and N. Roth, Constraints on Primordial Non-Gaussianity from 800 000 Photometric Quasars, Phys. Rev. Lett. 113 (2014) 221301 [1405.4315].
- [11] G. Cabass, M. M. Ivanov, O. H. E. Philcox, M. Simonović and M. Zaldarriaga, Constraints on Multi-Field Inflation from the BOSS Galaxy Survey, 2204.01781.
- [12] G. D'Amico, M. Lewandowski, L. Senatore and P. Zhang, Limits on primordial non-Gaussianities from BOSS galaxy-clustering data, 2201.11518.
- [13] M. Rezaie et al., Local primordial non-Gaussianity from the large-scale clustering of photometric DESI luminous red galaxies, Mon. Not. Roy. Astron. Soc. 532 (2024) 1902 [2307.01753].
- [14] DESI collaboration, Constraining primordial non-Gaussianity from DESI quasar targets and Planck CMB lensing, JCAP 03 (2024) 021 [2305.07650].
- [15] A. Barreira, Can we actually constrain f<sub>NL</sub> using the scale-dependent bias effect? An illustration of the impact of galaxy bias uncertainties using the BOSS DR12 galaxy power spectrum, J. Cosmology Astropart. Phys. 2022 (2022) 013 [2205.05673].
- [16] M. S. Cagliari, E. Castorina, M. Bonici and D. Bianchi, Optimal constraints on Primordial non-Gaussianity with the eBOSS DR16 quasars in Fourier space, JCAP 08 (2024) 036 [2309.15814].

- [17] F. McCarthy, M. S. Madhavacheril and A. S. Maniyar, Constraints on primordial non-Gaussianity from halo bias measured through CMB lensing cross-correlations, Phys. Rev. D 108 (2023) 083522 [2210.01049].
- [18] E. Chaussidon et al., Constraining primordial non-Gaussianity with DESI 2024 LRG and QSO samples, JCAP 06 (2025) 029 [2411.17623].
- [19] J. R. Bermejo-Climent et al., Constraints on primordial non-Gaussianity from the cross-correlation of DESI luminous red galaxies and Planck CMB lensing, Astron. Astrophys. 698 (2025) A177 [2412.10279].
- [20] G. Fabbian, D. Alonso, K. Storey-Fisher and T. Cornish, Constraints on primordial non-Gaussianity from Quaia, 2504.20992.
- [21] C. Cheung, P. Creminelli, A. L. Fitzpatrick, J. Kaplan and L. Senatore, *The Effective Field Theory of Inflation*, *JHEP* 03 (2008) 014 [0709.0293].
- [22] C. Cheung, A. L. Fitzpatrick, J. Kaplan and L. Senatore, On the consistency relation of the 3-point function in single field inflation, JCAP 02 (2008) 021 [0709.0295].
- [23] G. Cabass, M. M. Ivanov, M. Lewandowski, M. Mirbabayi and M. Simonović, Snowmass white paper: Effective field theories in cosmology, Physics of the Dark Universe 40 (2023) 101193 [2203.08232].
- [24] A. J. Tolley and M. Wyman, The Gelaton Scenario: Equilateral non-Gaussianity from multi-field dynamics, Phys. Rev. D 81 (2010) 043502 [0910.1853].
- [25] D. Green, B. Horn, L. Senatore and E. Silverstein, Trapped Inflation, Phys. Rev. D 80 (2009) 063533 [0902.1006].
- [26] G. Cabass, M. M. Ivanov, O. H. E. Philcox,
   M. Simonovic and M. Zaldarriaga, Constraining Single-Field Inflation with MegaMapper, 2211.14899.
- [27] O. H. E. Philcox, M. M. Ivanov, G. Cabass, M. Simonović, M. Zaldarriaga and T. Nishimichi, Cosmology with the redshift-space galaxy bispectrum monopole at one-loop order, Phys. Rev. D 106 (2022) 043530 [2206.02800].
- [28] S.-F. Chen, P. Chakraborty and C. Dvorkin, Analysis of BOSS galaxy data with weighted skew-spectra, JCAP 05 (2024) 011 [2401.13036].
- [29] M. M. Ivanov, C. Cuesta-Lazaro, S. Mishra-Sharma, A. Obuljen and M. W. Toomey, Full-shape analysis with simulation-based priors: Constraints on single field inflation from BOSS, Phys. Rev. D 110 (2024) 063538 [2402.13310].
- [30] J. Gleyzes, R. de Putter, D. Green and O. Doré, Biasing and the search for primordial non-Gaussianity beyond the local type, JCAP 04 (2017) 002 [1612.06366].
- [31] F. Schmidt and M. Kamionkowski, Halo Clustering with Non-Local Non-Gaussianity, Phys. Rev. D 82 (2010) 103002 [1008.0638].
- [32] F. Schmidt, D. Jeong and V. Desjacques, Peak-background split, renormalization, and galaxy clustering, Phys. Rev. D 88 (2013) 023515 [1212.0868].
- [33] R. Scoccimarro, L. Hui, M. Manera and K. C. Chan, Large-scale Bias and Efficient Generation of Initial Conditions for Non-Local Primordial Non-Gaussianity,

- Phys. Rev. D 85 (2012) 083002 [1108.5512].
- [34] M. Biagetti, T. Lazeyras, T. Baldauf, V. Desjacques and F. Schmidt, Verifying the consistency relation for the scale-dependent bias from local primordial non-Gaussianity, Mon. Not. Roy. Astron. Soc. 468 (2017) 3277 [1611.04901].
- [35] V. Desjacques, D. Jeong and F. Schmidt, Large-Scale Galaxy Bias, Phys. Rept. 733 (2018) 1 [1611.09787].
- [36] S. Goldstein, O. H. E. Philcox, J. C. Hill and L. Hui, Intermediate mass-range particles from small scales: Nonperturbative techniques for cosmological collider physics from large-scale structure surveys, Phys. Rev. D 110 (2024) 083516 [2407.08731].
- [37] V. Desjacques and U. Seljak, Primordial non-Gaussianity from the large-scale structure, Classical and Quantum Gravity 27 (2010) 124011 [1003.5020].
- [38] V. Assassi, D. Baumann and F. Schmidt, Galaxy Bias and Primordial Non-Gaussianity, JCAP 12 (2015) 043 [1510.03723].
- [39] T. Baldauf, U. Seljak, L. Senatore and M. Zaldarriaga, Galaxy bias and non-linear structure formation in general relativity, J. Cosmology Astropart. Phys. 2011 (2011) 031 [1106.5507].
- [40] L. Lucie-Smith, A. Barreira and F. Schmidt, Halo assembly bias from a deep learning model of halo formation, MNRAS 524 (2023) 1746 [2304.09880].
- [41] T. Lazeyras, A. Barreira, F. Schmidt and V. Desjacques, Assembly bias in the local PNG halo bias and its implication for f<sub>NL</sub> constraints, arXiv e-prints (2022) arXiv:2209.07251 [2209.07251].
- [42] S. Matarrese and L. Verde, The Effect of Primordial Non-Gaussianity on Halo Bias, ApJ 677 (2008) L77 [0801.4826].
- [43] E. Sefusatti and E. Komatsu, Bispectrum of galaxies from high-redshift galaxy surveys: Primordial non-Gaussianity and nonlinear galaxy bias, Phys. Rev. D 76 (2007) 083004 [0705.0343].
- [44] A. Pillepich, C. Porciani and O. Hahn, Halo mass function and scale-dependent bias from N-body simulations with non-Gaussian initial conditions, MNRAS 402 (2010) 191 [0811.4176].
- [45] V. Desjacques, U. Seljak and I. T. Iliev, Scale-dependent bias induced by local non-Gaussianity: a comparison to N-body simulations, MNRAS 396 (2009) 85 [0811.2748].
- [46] N. Afshordi and A. J. Tolley, Primordial non-Gaussianity, statistics of collapsed objects, and the integrated Sachs-Wolfe effect, Phys. Rev. D 78 (2008) 123507 [0806.1046].
- [47] R. Scoccimarro, E. Sefusatti and M. Zaldarriaga, Probing primordial non-Gaussianity with large-scale structure, Phys. Rev. D 69 (2004) 103513 [astro-ph/0312286].
- [48] M. Grossi, L. Verde, C. Carbone, K. Dolag, E. Branchini, F. Iannuzzi et al., Large-scale non-Gaussian mass function and halo bias: tests on N-body simulations, MNRAS 398 (2009) 321 [0902.2013].
- [49] D. Jeong and E. Komatsu, Primordial Non-Gaussianity, Scale-dependent Bias, and the Bispectrum of Galaxies, ApJ 703 (2009) 1230 [0904.0497].

- [50] P. McDonald, Primordial non-Gaussianity: Large-scale structure signature in the perturbative bias model, Phys. Rev. D 78 (2008) 123519 [0806.1061].
- [51] T. Giannantonio and C. Porciani, Structure formation from non-Gaussian initial conditions: Multivariate biasing, statistics, and comparison with N-body simulations, Phys. Rev. D 81 (2010) 063530 [0911.0017].
- [52] L. Verde and S. Matarrese, Detectability of the Effect of Inflationary Non-Gaussianity on Halo Bias, ApJ 706 (2009) L91 [0909.3224].
- [53] F. Schmidt and M. Kamionkowski, Halo clustering with nonlocal non-Gaussianity, Phys. Rev. D 82 (2010) 103002 [1008.0638].
- [54] V. Desjacques, D. Jeong and F. Schmidt, Non-Gaussian Halo Bias Re-examined: Mass-dependent Amplitude from the Peak-Background Split and Thresholding, Phys. Rev. D 84 (2011) 063512 [1105.3628].
- [55] K. M. Smith, S. Ferraro and M. LoVerde, *Halo clustering and g\_{NL}-type primordial non-gaussianity*, J. Cosmology Astropart. Phys. **2012** (2012) 032 [1106.0503].
- [56] W. R. Coulton, F. Villaescusa-Navarro, D. Jamieson, M. Baldi, G. Jung, D. Karagiannis et al., Quijote-PNG: The Information Content of the Halo Power Spectrum and Bispectrum, ApJ 943 (2023) 178 [2206.15450].
- [57] A. Barreira, The local PNG bias of neutral Hydrogen, H<sub>I</sub>, J. Cosmology Astropart. Phys. 2022 (2022) 057 [2112.03253].
- [58] P. McDonald, Primordial non-Gaussianity: Large-scale structure signature in the perturbative bias model, Phys. Rev. D 78 (2008) 123519 [0806.1061].
- [59] A. G. Adame, S. Avila, V. Gonzalez-Perez, G. Yepes, M. Pellejero, M. S. Wang et al., PNG-UNITsims: Halo clustering response to primordial non-Gaussianities as a function of mass, arXiv e-prints (2023) arXiv:2312.12405 [2312.12405].
- [60] A. Gutiérrez Adame, S. Avila, V. Gonzalez-Perez, G. Yepes, M. Pellejero, M. S. Wang et al., PNG-UNITsims: Halo clustering response to primordial non-Gaussianities as a function of mass, A&A 689 (2024) A69 [2312.12405].
- [61] B. Hadzhiyska, L. H. Garrison, D. J. Eisenstein and S. Ferraro, Modest set of simulations of local-type primordial non-Gaussianity in the DESI era, Phys. Rev. D 109 (2024) 103530 [2402.10881].
- [62] B. Hadzhiyska and S. Ferraro, Refining localtype primordial non-Gaussianity: Sharpened bφ constraints through bias expansion, Phys. Rev. D 111 (2025) 103521 [2501.14873].
- [63] T. Lazeyras, A. Barreira and F. Schmidt, Assembly bias in quadratic bias parameters of dark matter halos from forward modeling, J. Cosmology Astropart. Phys. 2021 (2021) 063 [2106.14713].
- [64] M. Marinucci, V. Desjacques and A. Benson, Non-Gaussian assembly bias from a semi-analytic galaxy formation model, MNRAS 524 (2023) 325 [2303.10337].
- [65] D. Ginzburg, V. Desjacques and K. C. Chan, Shot noise and biased tracers: A new look at the halo model, Phys. Rev. D 96 (2017) 083528 [1706.08738].

- [66] J. M. Sullivan and S.-F. Chen, Local primordial non-Gaussian bias at the field level, JCAP 03 (2025) 016 [2410.18039].
- [67] J. M. Sullivan and U. Seljak, Local primordial non-Gaussian bias from time evolution, Phys. Rev. D 112 (2025) 083522 [2503.21736].
- [68] C. Shiveshwarkar, M. Loverde, C. M. Hirata and D. Jamieson, Where does non-Universality in Assembly Bias come from?, arXiv e-prints (2025) arXiv:2508.11798 [2508.11798].
- [69] V. Desjacques, D. Jeong and F. Schmidt, Non-Gaussian Halo Bias Re-examined: Mass-dependent Amplitude from the Peak-Background Split and Thresholding, Phys. Rev. D 84 (2011) 063512 [1105.3628].
- [70] M. LoVerde, A. Miller, S. Shandera and L. Verde, Effects of scale-dependent non-Gaussianity on cosmological structures, J. Cosmology Astropart. Phys. 2008 (2008) 014 [0711.4126].
- [71] T. Lazeyras and F. Schmidt, A robust measurement of the first higher-derivative bias of dark matter halos, 1904.11294.
- [72] M. M. Ivanov, A. Obuljen, C. Cuesta-Lazaro and M. W. Toomey, Full-shape analysis with simulation-based priors: cosmological parameters and the structure growth anomaly, 2409.10609.
- [73] M. M. Ivanov, Simulation-Based Priors without Simulations: an Analytic Perspective on EFT Parameters of Galaxies, 2503.07270.
- [74] P. McDonald and A. Roy, Clustering of dark matter tracers: generalizing bias for the coming era of precision LSS, JCAP 0908 (2009) 020 [0902.0991].
- [75] D. Baumann, A. Nicolis, L. Senatore and M. Zaldarriaga, Cosmological Non-Linearities as an Effective Fluid, JCAP 1207 (2012) 051 [1004.2488].
- [76] M. M. Ivanov, Effective Field Theory for Large Scale Structure, 2212.08488.
- [77] M. M. Ivanov, M. Simonović and M. Zaldarriaga, Cosmological Parameters from the BOSS Galaxy Power Spectrum, JCAP 05 (2020) 042 [1909.05277].
- [78] A. Chudaykin, M. M. Ivanov, O. H. E. Philcox and M. Simonović, Nonlinear perturbation theory extension of the Boltzmann code CLASS, Phys. Rev. D 102 (2020) 063533 [2004.10607].
- [79] S.-F. Chen, Z. Vlah and M. White, Consistent Modeling of Velocity Statistics and Redshift-Space Distortions in One-Loop Perturbation Theory, JCAP 07 (2020) 062 [2005.00523].
- [80] S.-F. Chen, Z. Vlah, E. Castorina and M. White, Redshift-Space Distortions in Lagrangian Perturbation Theory, JCAP 03 (2021) 100 [2012.04636].
- [81] S.-F. Chen, Z. Vlah and M. White, A new analysis of galaxy 2-point functions in the BOSS survey, including full-shape information and post-reconstruction BAO, JCAP 02 (2022) 008 [2110.05530].
- [82] G. D'Amico, L. Senatore and P. Zhang, Limits on wCDM from the EFTofLSS with the PyBird code, JCAP **01** (2021) 006 [2003.07956].
- [83] D. Linde, A. Moradinezhad Dizgah, C. Radermacher, S. Casas and J. Lesgourgues, CLASS-OneLoop: accurate and unbiased inference from spectroscopic galaxy surveys, JCAP 07 (2024) 068 [2402.09778].
- [84] H. E. Noriega, A. Aviles, S. Fromenteau and M. Vargas-Magaña, Fast computation of non-linear

- power spectrum in cosmologies with massive neutrinos, JCAP 11 (2022) 038 [2208.02791].
- [85] C. Moretti, M. Tsedrik, P. Carrilho and A. Pourtsidou, Modified gravity and massive neutrinos: constraints from the full shape analysis of BOSS galaxies and forecasts for Stage IV surveys, JCAP 12 (2023) 025 [2306.09275].
- [86] A. Barreira, On the impact of galaxy bias uncertainties on primordial non-Gaussianity constraints, JCAP 12 (2020) 031 [2009.06622].
- [87] A. Barreira, T. Lazeyras and F. Schmidt, Galaxy bias from forward models: linear and second-order bias of IllustrisTNG galaxies, 2105.02876.
- [88] A. Barreira, Predictions for local PNG bias in the galaxy power spectrum and bispectrum and the consequences for f<sub>NL</sub> constraints, J. Cosmology Astropart. Phys. 2022 (2022) 033 [2107.06887].
- [89] E. Fondi, L. Verde, F. Villaescusa-Navarro, M. Baldi, W. R. Coulton, G. Jung et al., Taming assembly bias for primordial non-Gaussianity, J. Cosmology Astropart. Phys. 2024 (2024) 048 [2311.10088].
- [90] V. Assassi, D. Baumann, D. Green and M. Zaldarriaga, Renormalized Halo Bias, JCAP 1408 (2014) 056 [1402.5916].
- [91] M. Schmittfull, M. Simonović, V. Assassi and M. Zaldarriaga, Modeling Biased Tracers at the Field Level, Phys. Rev. D 100 (2019) 043514 [1811.10640].
- [92] M. Schmittfull, M. Simonović, M. M. Ivanov, O. H. E. Philcox and M. Zaldarriaga, Modeling Galaxies in Redshift Space at the Field Level, JCAP 05 (2021) 059 [2012.03334].
- [93] A. Obuljen, M. Simonović, A. Schneider and R. Feldmann, Modeling HI at the field level, Phys. Rev. D 108 (2023) 083528 [2207.12398].
- [94] S. Foreman, A. Obuljen and M. Simonović, Improving cosmological analyses of HI clustering by reducing stochastic noise, 2405.18559.
- [95] M. Schmittfull, T. Baldauf and U. Seljak, Near optimal bispectrum estimators for large-scale structure, Phys. Rev. D 91 (2015) 043530 [1411.6595].
- [96] T. Lazeyras and F. Schmidt, Beyond LIMD bias: a measurement of the complete set of third-order halo bias parameters, JCAP 1809 (2018) 008 [1712.07531].
- [97] M. M. Abidi and T. Baldauf, Cubic Halo Bias in Eulerian and Lagrangian Space, JCAP 1807 (2018) 029 [1802.07622].
- [98] F. Schmidt, F. Elsner, J. Jasche, N. M. Nguyen and G. Lavaux, A rigorous EFT-based forward model for large-scale structure, JCAP 01 (2019) 042 [1808.02002].
- [99] F. Elsner, F. Schmidt, J. Jasche, G. Lavaux and N.-M. Nguyen, Cosmology inference from a biased density field using the EFT-based likelihood, JCAP 01 (2020) 029 [1906.07143].
- [100] G. Cabass and F. Schmidt, The EFT Likelihood for Large-Scale Structure, JCAP 04 (2020) 042 [1909.04022].
- [101] C. Modi, S.-F. Chen and M. White, Simulations and symmetries, Mon. Not. Roy. Astron. Soc. 492 (2020) 5754 [1910.07097].
- [102] F. Schmidt, Sigma-Eight at the Percent Level: The EFT Likelihood in Real Space, 2009.14176.
- [103] F. Schmidt, G. Cabass, J. Jasche and G. Lavaux, Unbiased Cosmology Inference from Biased Tracers

- using the EFT Likelihood, JCAP 11 (2020) 008 [2004.06707].
- [104] T. Lazeyras, A. Barreira and F. Schmidt, Assembly bias in quadratic bias parameters of dark matter halos from forward modeling, JCAP 10 (2021) 063 [2106.14713].
- [105] J. Stadler, F. Schmidt and M. Reinecke, Cosmology inference at the field level from biased tracers in redshift-space, JCAP 10 (2023) 069 [2303.09876].
- [106] K. Akitsu, Y. Li and T. Okumura, Quadratic shape biases in three-dimensional halo intrinsic alignments, JCAP 08 (2023) 068 [2306.00969].
- [107] N.-M. Nguyen, F. Schmidt, B. Tucci, M. Reinecke and A. Kostić, How much information can be extracted from galaxy clustering at the field level?, 2403.03220.
- [108] K. Akitsu, Mapping the galaxy-halo connection to the galaxy bias: implication to the HOD-informed prior, 2410.08998.
- [109] K. Akitsu, M. Simonović, S.-F. Chen, G. Cabass and M. Zaldarriaga, Cosmology inference with perturbative forward modeling at the field level: a comparison with joint power spectrum and bispectrum analyses, 2509.09673.
- [110] M. M. Ivanov et al., The Millennium and Astrid galaxies in effective field theory: comparison with galaxy-halo connection models at the field level, 2412.01888.
- [111] X. Chen, Primordial Non-Gaussianities from Inflation Models, Adv. Astron. 2010 (2010) 638979 [1002.1416].
- [112] J. M. Bardeen, Gauge-invariant cosmological perturbations, Phys. Rev. D 22 (1980) 1882.
- [113] N. Bartolo, E. Komatsu, S. Matarrese and A. Riotto, Non-gaussianity from inflation: theory and observations. Physics Reports 402 (2004) 103–266.
- [114] P. D. Meerburg, D. Green, R. Flauger, B. Wallisch, M. C. D. Marsh, E. Pajer et al., *Primordial Non-Gaussianity*, BAAS 51 (2019) 107 [1903.04409].
- [115] X. Chen, Primordial Non-Gaussianities from Inflation Models, Advances in Astronomy 2010 (2010) 638979 [1002.1416].
- [116] L. Senatore, K. M. Smith and M. Zaldarriaga, Non-Gaussianities in Single Field Inflation and their Optimal Limits from the WMAP 5-year Data, JCAP 01 (2010) 028 [0905.3746].
- [117] Planck Collaboration, N. Aghanim and A. Zonca, Planck 2018 results. VI. Cosmological parameters, A&A 641 (2020) A6 [1807.06209].
- [118] V. Desjacques, D. Jeong and F. Schmidt, Accurate Predictions for the Scale-Dependent Galaxy Bias from Primordial Non-Gaussianity, Phys. Rev. D 84 (2011) 061301 [1105.3476].
- [119] V. Assassi, D. Baumann, E. Pajer, Y. Welling and D. van der Woude, Effective theory of large-scale structure with primordial non-Gaussianity, JCAP 11 (2015) 024 [1505.06668].
- [120] M. M. Ivanov, C. Cuesta-Lazaro, S. Mishra-Sharma, A. Obuljen and M. W. Toomey, Full-shape analysis with simulation-based priors: Constraints on single field inflation from BOSS, Phys. Rev. D 110 (2024) 063538 [2402.13310].
- [121] M. M. Ivanov, A. Obuljen, C. Cuesta-Lazaro and M. W. Toomey, Full-shape analysis with simulation-based priors: cosmological parameters and the structure growth anomaly, arXiv e-prints (2024)

- arXiv:2409.10609 [2409.10609].
- [122] J. M. Sullivan, C. Cuesta-Lazaro, M. M. Ivanov, Y. Ni, S. Bose, B. Hadzhiyska et al., High-redshift millennium and astrid galaxies in effective field theory at the field level, Phys. Rev. D 112 (2025) 083521 [2505.03626].
- [123] R. de Belsunce, M. M. Ivanov, J. M. Sullivan, K. Akitsu and S.-F. Chen, Modeling the Cosmological Lyman-α Forest at the Field Level, arXiv e-prints (2025) arXiv:2507.00284 [2507.00284].
- [124] G. Cabass, M. Simonović and M. Zaldarriaga, Cosmological information in perturbative forward modeling, Phys. Rev. D 109 (2024) 043526 [2307.04706].
- [125] F. Schmidt, F. Elsner, J. Jasche, N. M. Nguyen and G. Lavaux, A rigorous EFT-based forward model for large-scale structure, J. Cosmology Astropart. Phys. 2019 (2019) 042 [1808.02002].
- [126] F. Schmidt, Sigma-eight at the percent level: the EFT likelihood in real space, J. Cosmology Astropart. Phys. 2021 (2021) 032 [2009.14176].
- [127] J. Stadler, F. Schmidt and M. Reinecke, Fast, Accurate and Perturbative Forward Modeling of Galaxy Clustering Part I: Galaxies in the Restframe, arXiv e-prints (2024) arXiv:2409.10937 [2409.10937].
- [128] N.-M. Nguyen, F. Schmidt, B. Tucci, M. Reinecke and A. Kostić, How Much Information Can Be Extracted from Galaxy Clustering at the Field Level?, Phys. Rev. Lett. 133 (2024) 221006 [2403.03220].
- [129] F. Spezzati, M. Marinucci and M. Simonović, Equivalence of the field-level inference and conventional analyses on large scales, arXiv e-prints (2025) arXiv:2507.05378 [2507.05378].
- [130] M. M. Ivanov, O. H. E. Philcox, T. Nishimichi, M. Simonović, M. Takada and M. Zaldarriaga, Precision analysis of the redshift-space galaxy bispectrum, Phys. Rev. D 105 (2022) 063512 [2110.10161].
- [131] T. Baldauf, U. Seljak, R. E. Smith, N. Hamaus and V. Desjacques, Halo stochasticity from exclusion and nonlinear clustering, Phys. Rev. D 88 (2013) 083507 [1305.2917].
- [132] J. M. Sullivan, U. Seljak and S. Singh, An analytic hybrid halo + perturbation theory model for small-scale correlators: baryons, halos, and galaxies, J. Cosmology Astropart. Phys. 2021 (2021) 026 [2104.10676].
- [133] N. Kokron, J. DeRose, S.-F. Chen, M. White and R. H. Wechsler, Priors on red galaxy stochasticity from hybrid effective field theory, MNRAS 514 (2022) 2198 [2112.00012].
- [134] T. Baldauf, S. Codis, V. Desjacques and C. Pichon, Peak exclusion, stochasticity and convergence of perturbative bias expansions in 1+1 gravity, Mon. Not. Roy. Astron. Soc. 456 (2016) 3985 [1510.09204].
- [135] D. Blas, M. Garny, M. M. Ivanov and S. Sibiryakov, Time-Sliced Perturbation Theory for Large Scale Structure I: General Formalism, JCAP 1607 (2016) 052 [1512.05807].
- [136] D. Blas, M. Garny, M. M. Ivanov and S. Sibiryakov, Time-Sliced Perturbation Theory II: Baryon Acoustic Oscillations and Infrared Resummation, JCAP 1607 (2016) 028 [1605.02149].
- [137] M. M. Ivanov and S. Sibiryakov, Infrared Resummation for Biased Tracers in Redshift Space, JCAP 1807 (2018) 053 [1804.05080].

- [138] A. Vasudevan, M. M. Ivanov, S. Sibiryakov and J. Lesgourgues, Time-sliced perturbation theory with primordial non-Gaussianity and effects of large bulk flows on inflationary oscillating features, JCAP 09 (2019) 037 [1906.08697].
- [139] M. Simonovic, T. Baldauf, M. Zaldarriaga, J. J. Carrasco and J. A. Kollmeier, Cosmological perturbation theory using the FFTLog: formalism and connection to QFT loop integrals, JCAP 1804 (2018) 030 [1708.08130].
- [140] M. Biagetti, T. Lazeyras, T. Baldauf, V. Desjacques and F. Schmidt, Verifying the consistency relation for the scale-dependent bias from local primordial non-Gaussianity, MNRAS 468 (2017) 3277 [1611.04901].
- [141] V. Springel, R. Pakmor, O. Zier and M. Reinecke, Simulating cosmic structure formation with the gadget-4 code, Mon. Not. Roy. Astron. Soc. 506 (2021) 2871 [2010.03567].
- [142] M. Crocce, S. Pueblas and R. Scoccimarro, Transients from Initial Conditions in Cosmological Simulations, Mon. Not. Roy. Astron. Soc. 373 (2006) 369 [astro-ph/0606505].
- [143] P. S. Behroozi, R. H. Wechsler and H.-Y. Wu, The Rockstar Phase-Space Temporal Halo Finder and the Velocity Offsets of Cluster Cores, Astrophys. J. 762 (2013) 109 [1110.4372].
- [144] F. Villaescusa-Navarro et al., The Quijote simulations, Astrophys. J. Suppl. 250 (2020) 2 [1909.05273].
- [145] V. Springel, The Cosmological simulation code GADGET-2, Mon. Not. Roy. Astron. Soc. 364 (2005) 1105 [astro-ph/0505010].
- [146] M. M. Ivanov, M. W. Toomey and N. G. Karaçaylı, Fundamental physics with the Lyman-alpha forest: constraints on the growth of structure and neutrino masses from SDSS with effective field theory, 2405.13208.
- [147] P. Valageas, Mass function and bias of dark matter halos for non-Gaussian initial conditions, Astron. Astrophys. 514 (2010) A46 [0906.1042].
- [148] J. L. Tinker, A. V. Kravtsov, A. Klypin, K. Abazajian, M. S. Warren, G. Yepes et al., Toward a halo mass function for precision cosmology: The Limits of universality, Astrophys. J. 688 (2008) 709 [0803.2706].
- [149] G. Jung, A. Ravenni, M. Baldi, W. R. Coulton, D. Jamieson, D. Karagiannis et al., Quijote-PNG: The Information Content of the Halo Mass Function, ApJ 957 (2023) 50 [2305.10597].
- [150] G. Cabass, M. M. Ivanov, O. H. E. Philcox, M. Simonović and M. Zaldarriaga, Constraints on

- Single-Field Inflation from the BOSS Galaxy Survey, 2201.07238.
- [151] W. H. Press and P. Schechter, Formation of galaxies and clusters of galaxies by selfsimilar gravitational condensation, Astrophys. J. 187 (1974) 425.
- [152] A. Chudaykin, M. M. Ivanov and O. H. E. Philcox, Reanalyzing DESI DR1: 1. ΛCDM Constraints from the Power Spectrum and Bispectrum, 2507.13433.
- [153] X. Chen and Y. Wang, Quasi-Single Field Inflation and Non-Gaussianities, JCAP 04 (2010) 027 [0911.3380].
- [154] X. Chen and Y. Wang, Large non-Gaussianities with Intermediate Shapes from Quasi-Single Field Inflation, Phys. Rev. D 81 (2010) 063511 [0909.0496].
- [155] D. Baumann and D. Green, Signatures of Supersymmetry from the Early Universe, Phys. Rev. D 85 (2012) 103520 [1109.0292].
- [156] N. Arkani-Hamed and J. Maldacena, Cosmological Collider Physics, 1503.08043.
- [157] A. Moradinezhad Dizgah and C. Dvorkin, Scale-Dependent Galaxy Bias from Massive Particles with Spin during Inflation, JCAP 01 (2018) 010 [1708.06473].
- [158] A. Moradinezhad Dizgah, H. Lee, J. B. Muñoz and C. Dvorkin, Galaxy Bispectrum from Massive Spinning Particles, JCAP 05 (2018) 013 [1801.07265].
- [159] A. Moradinezhad Dizgah, H. Lee, M. Schmittfull and C. Dvorkin, Capturing non-Gaussianity of the large-scale structure with weighted skew-spectra, JCAP 04 (2020) 011 [1911.05763].
- [160] A. Moradinezhad Dizgah, M. Biagetti, E. Sefusatti, V. Desjacques and J. Noreña, Primordial Non-Gaussianity from Biased Tracers: Likelihood Analysis of Real-Space Power Spectrum and Bispectrum, JCAP 05 (2021) 015 [2010.14523].
- [161] S. Kumar and R. Sundrum, Seeing Higher-Dimensional Grand Unification In Primordial Non-Gaussianities, JHEP 04 (2019) 120 [1811.11200].
- [162] S. Kumar and R. Sundrum, Cosmological Collider Physics and the Curvaton, JHEP 04 (2020) 077 [1908.11378].
- [163] M. Reece, L.-T. Wang and Z.-Z. Xianyu, Large-Field Inflation and the Cosmological Collider, 2204.11869.
- [164] G. Cabass, M. M. Ivanov and O. H. E. Philcox, Colliders and ghosts: Constraining inflation with the parity-odd galaxy four-point function, Phys. Rev. D 107 (2023) 023523 [2210.16320].
- [165] G. Cabass, O. H. E. Philcox, M. M. Ivanov, K. Akitsu, S.-F. Chen, M. Simonović et al., BOSS Constraints on Massive Particles during Inflation: The Cosmological Collider in Action, 2404.01894.